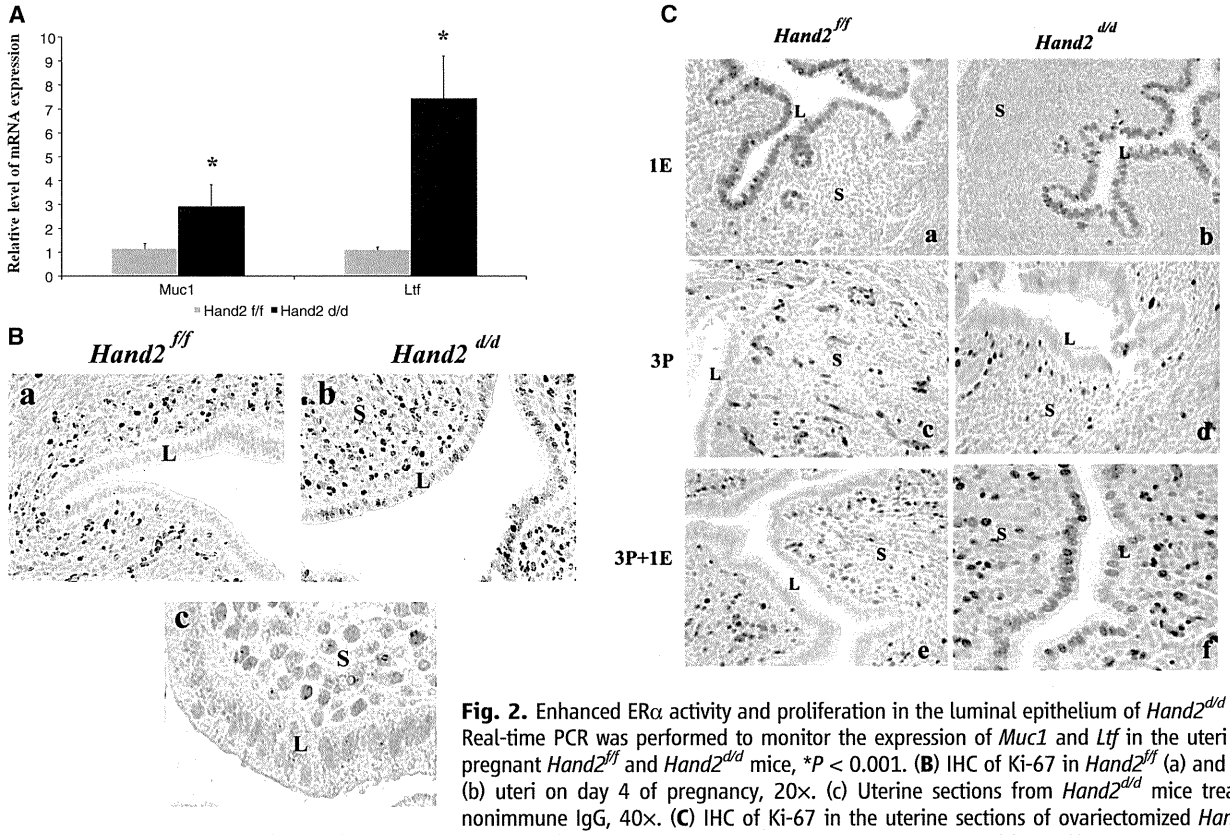

Fig. 2. Enhanced ERα activity and proliferation in the luminal epithelium of *Hand2*$^{d/d}$ uteri. (**A**) Real-time PCR was performed to monitor the expression of *Muc1* and *Ltf* in the uteri of day 4 pregnant *Hand2*$^{f/f}$ and *Hand2*$^{d/d}$ mice, *$P < 0.001$. (**B**) IHC of Ki-67 in *Hand2*$^{f/f}$ (a) and *Hand2*$^{d/d}$ (b) uteri on day 4 of pregnancy, 20×. (c) Uterine sections from *Hand2*$^{d/d}$ mice treated with nonimmune IgG, 40×. (**C**) IHC of Ki-67 in the uterine sections of ovariectomized *Hand2*$^{f/f}$ and *Hand2*$^{d/d}$ mice treated with E for 1 day (a) and (b), P for 3 days (c) and (d), or 2 days of P treatment followed by P and E (e) and (f).

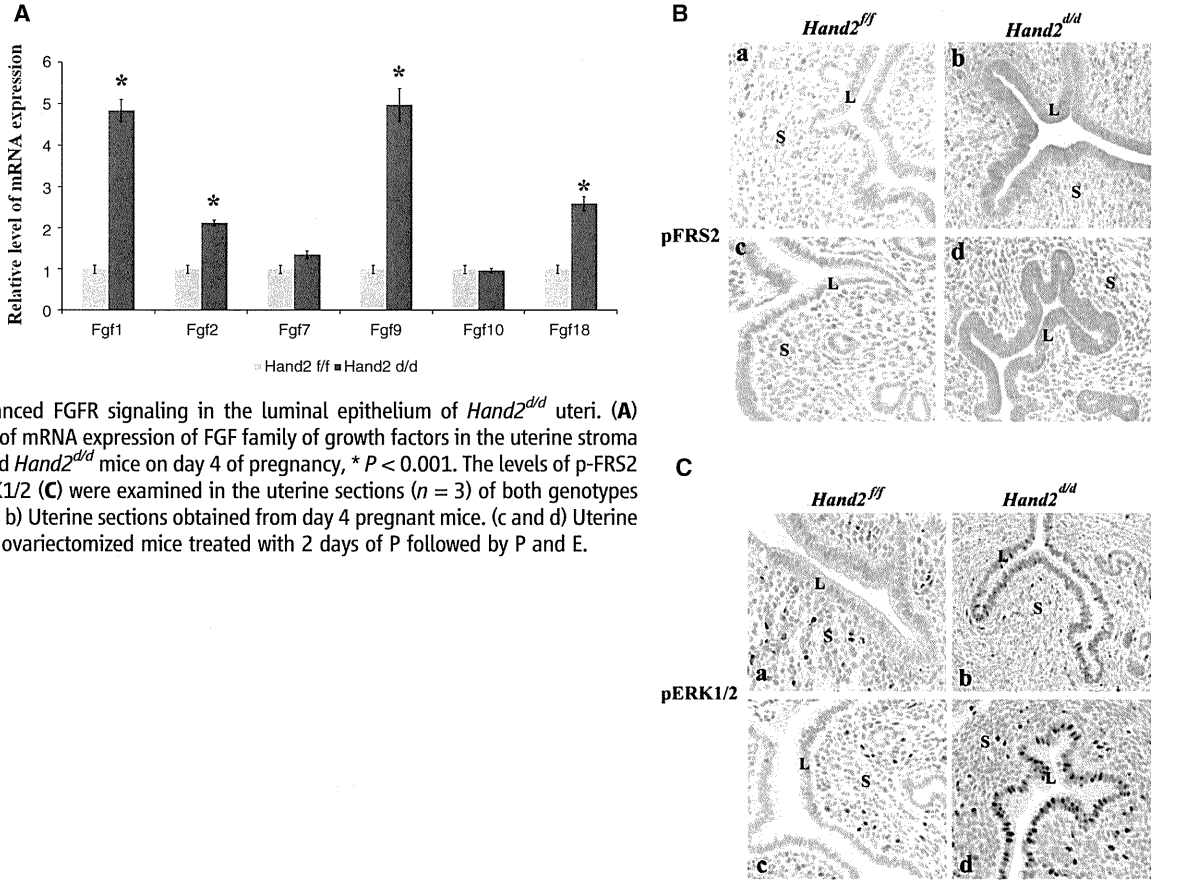

Fig. 3. Enhanced FGFR signaling in the luminal epithelium of *Hand2*$^{d/d}$ uteri. (**A**) Relative level of mRNA expression of FGF family of growth factors in the uterine stroma of *Hand2*$^{f/f}$ and *Hand2*$^{d/d}$ mice on day 4 of pregnancy, * $P < 0.001$. The levels of p-FRS2 (**B**) and p-ERK1/2 (**C**) were examined in the uterine sections ($n = 3$) of both genotypes by IHC. (a and b) Uterine sections obtained from day 4 pregnant mice. (c and d) Uterine sections from ovariectomized mice treated with 2 days of P followed by P and E.

docking protein complex (*14*). FGF-stimulation of FGFRs induces phosphorylation of specific tyrosine residues in a critical docking protein, FGFR substrate2 (FRS2), which guides the assembly of distinct multiprotein complexes, leading to activation of either extracellular signal–regulated kinase (ERK) 1 and 2 (ERK1/2) or phosphatidylinositol 3-kinase/Akt (PI3K/Akt) signaling cascades (*14*). We determined the expression of FGFRs 1 and 2 in uteri on days 1 and 4 of pregnancy and found that these receptors localized to the epithelium (fig. S12A). The levels of mRNAs corresponding to *Fgfr 1* to *3* were comparable in uteri of *Hand2*$^{f/f}$ and *Hand2*$^{d/d}$ mice on day 4 of pregnancy (fig. S12B).

The activation of the FGFR signaling pathway in uteri of *Hand2*$^{f/f}$ and *Hand2*$^{d/d}$ mice was monitored by examining the tyrosine phosphorylation status of FRS2. Whereas only low levels of phospho-FRS2 were seen in the uterine epithelium of *Hand2*$^{f/f}$ mice on day 4 of pregnancy (Fig. 3B, a), a marked increase in its level was observed in the epithelium of *Hand2*-null uteri, indicating that FGF signaling is activated in the absence of Hand2 (Fig. 3B, b). Phospho-FRS2 was undetectable in uterine epithelium of ovariectomized *Hand2*$^{f/f}$ mice in which P effectively blocks E-mediated proliferation (Fig. 3B, c). However, the epithelial cells of *Hand2*-null uteri, which showed proliferative activity under similar hormone treatment conditions, exhibited a marked elevation in the level of phospho-FRS2, reflecting the activation of FGFR signaling in these cells (Fig. 3B, d). We also monitored the activated phosphorylated states of ErbB1 and ErbB4, the primary receptors mediating the actions of *Hbegf* (*15*). The activated forms of these receptors were undetectable in uterine epithelia of *Hand2*$^{f/f}$ *and Hand2*$^{d/d}$ mice on day 4 of gestation (fig. S13), which indicated that the increased HB-EGF produced by the stroma of *Hand2*-null uteri did not act directly on the epithelial cells.

We next investigated whether the ERK1/2 and/or PI3K/Akt signaling pathways were activated downstream of FGFR in the epithelia of *Hand2*-ablated uteri. As shown in Fig. 3C, an increase in the level of phospho-ERK1/2 was seen in uterine epithelium of *Hand2*-null mice on day 4 of pregnancy (Fig. 3C, b) and also in response to E treatment in the presence of P (Fig. 3C, d). In contrast, the phospho-AKT levels were undetectable or low and remained unaltered in the uterine epithelia of these mice (fig. S14), which suggested that the ERK1/2 pathway, but not the PI3K/Akt pathway, is the key downstream mediator of enhanced FGF signaling in *Hand2*-null uteri.

To examine whether the elevated mitogenic activity in the luminal epithelium of *Hand2*$^{d/d}$ uteri is induced by FGF and ERK1/2 signaling, we administered PD173074 [a FGFR-specific inhibitor (*16*)] or vehicle into uterine horns of *Hand2*$^{d/d}$ mice at the time of implantation. The epithelia of vehicle-treated horn showed prominent expression of p-FRS2 and p-ERK1/2 (Fig. 4A, a and c). However, the levels of both p-FRS2 and p-ERK1/2 were reduced in the epithelia of PD173074-treated horn on day 4 of pregnancy (Fig. 4A, b and d). We also observed a marked decline in the proliferative activity of *Hand2*-null uterine epithelia, as indicated by decreased Ki-67 staining (Fig. 4A, e and f). In parallel experiments, administration of PD184352, an inhibitor of the ERK1/2 pathway (*17*), to uterine horns of *Hand2*$^{d/d}$ mice suppressed the level of pERK1/2 (Fig. 4B, a and b), as well as luminal epithelial

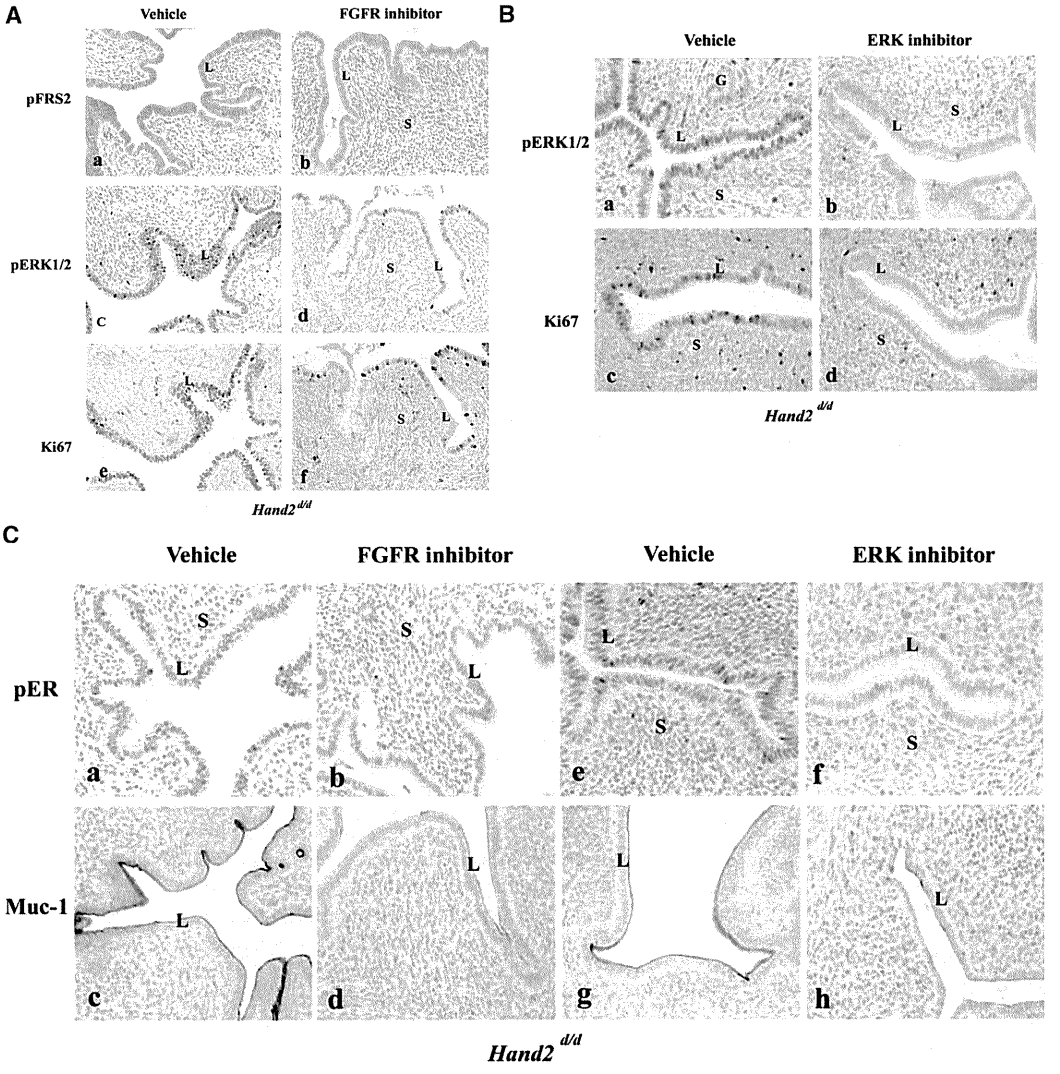

Fig. 4. The inhibitor PD173074 (**A**) or PD184352 (**B**) was administered to one uterine horn of Hand2$^{d/d}$ mice on day 3 of pregnancy (n = 5). The other horn served as vehicle-treated control. Uterine horns were collected on the morning of day 4, and sections were subjected to IHC to detect p-FRS2, p-ERK1/2, and Ki-67. (**C**) IHC of pERα and Muc-1 in uterine sections of Hand2$^{d/d}$ mice treated with PD173074 or PD184352.

proliferation (Fig. 4B, c and d). Collectively these results are consistent with the hypothesis that increased FGF production by the *Hand2*-null uterine stroma stimulates epithelial proliferation by activating the FGFR-ERK1/2 pathway.

The ERK1/2-dependent phosphorylation of epithelial ERα at Ser^{118} is critical for the transcriptional activation of ERα (*11*). Administration of either PD173074 (Fig. 4C, a to d) or PD184352 (Fig. 4C, e to h) to *Hand2*-null uterine horns blocked the phosphorylation of epithelial ERα at Ser^{118} and the expression of Muc-1. This result supported our view that elevated signaling by FGFR-ERK1/2 pathway in $Hand2^{d/d}$ uteri is responsible for phosphorylation and activation of ERα in epithelial cells, which promotes persistent expression of Muc-1 and which in turn creates a barrier that prevents embryo attachment.

Earlier studies using tissue recombinants prepared with uterine epithelium and stroma isolated from neonatal wild-type and PR-null mice indicated that the stromal PR plays an obligatory role in mediating the inhibitory actions of P on E-induced epithelial cell proliferation (*18*). However, the mechanism of this stromal-epithelial communication remained unknown. Our study has delineated a pathway in which Hand2 operates downstream of P to regulate the production of FGFs, mitogenic paracrine signals that originate in the stroma and act on the FGFR(s) in epithelium to control its E responsiveness (fig. S15). The antiproliferative action of P in uterine epithelium is of clinical significance, because the breakdown of this action underpins E-dependent endometrial cancer (*19*). Hand2, therefore, is an important factor to be considered for hormone therapy to block the proliferative actions of E in the endometrium.

References and Notes

1. C. A. Finn, L. Martin, *J. Reprod. Fertil.* **39**, 195 (1974).
2. D. D. Carson *et al.*, *Dev. Biol.* **223**, 217 (2000).
3. C. Y. Ramathal, I. C. Bagchi, R. N. Taylor, M. K. Bagchi, *Semin. Reprod. Med.* **28**, 17 (2010).
4. L. Martin, R. M. Das, C. A. Finn, *J. Endocrinol.* **57**, 549 (1973).
5. I. C. Bagchi, Y. P. Cheon, Q. Li, M. K. Bagchi, *Front. Biosci.* **8**, s852 (2003).
6. H. Pan, Y. Deng, J. W. Pollard, *Proc. Natl. Acad. Sci. U.S.A.* **103**, 14021 (2006).
7. I. C. Bagchi *et al.*, *Semin. Reprod. Med.* **23**, 38 (2005).
8. D. Srivastava *et al.*, *Nat. Genet.* **16**, 154 (1997).
9. A. B. Firulli, *Gene* **312**, 27 (2003).
10. Materials and methods are available as supporting material on *Science* Online.
11. S. Kato *et al.*, *Science* **270**, 1491 (1995).
12. G. A. Surveyor *et al.*, *Endocrinology* **136**, 3639 (1995).
13. K. Y. Lee *et al.*, *Nat. Genet.* **38**, 1204 (2006).
14. V. P. Eswarakumar, I. Lax, J. Schlessinger, *Cytokine Growth Factor Rev.* **16**, 139 (2005).
15. R. Iwamoto, E. Mekada, *Cytokine Growth Factor Rev.* **11**, 335 (2000).
16. M. Koziczak, T. Holbro, N. E. Hynes, *Oncogene* **23**, 3501 (2004).
17. D. B. Solit *et al.*, *Nature* **439**, 358 (2006).
18. T. Kurita *et al.*, *Endocrinology* **139**, 4708 (1998).
19. J. J. Kim, E. Chapman-Davis, *Semin. Reprod. Med.* **28**, 81 (2010).

20. We thank M. Laws for genotyping and Y. Li for immunohistochemistry. This work was supported by the Eunice Kennedy Shriver National Institute of Child Health and Human Development, NIH, through U54HD055787 as part of the Specialized Cooperative Centers Program in Reproduction and Infertility Research. The Gene Expression Omnibus (GEO) microarray accession number is GSE25881.

Supporting Online Material

www.sciencemag.org/cgi/content/full/331/6019/912/DC1
Materials and Methods
Figs. S1 to S15
Table S1
References

7 September 2010; accepted 15 December 2010
10.1126/science.1197454

Distinct Properties of the XY Pseudoautosomal Region Crucial for Male Meiosis

Liisa Kauppi,[1] Marco Barchi,[2,3] Frédéric Baudat,[2]* Peter J. Romanienko,[2] Scott Keeney,[1,4]† Maria Jasin[2]†

Meiosis requires that each chromosome find its homologous partner and undergo at least one crossover. X-Y chromosome segregation hinges on efficient crossing-over in a very small region of homology, the pseudoautosomal region (PAR). We find that mouse PAR DNA occupies unusually long chromosome axes, potentially as shorter chromatin loops, predicted to promote double-strand break (DSB) formation. Most PARs show delayed appearance of RAD51/DMC1 foci, which mark DSB ends, and all PARs undergo delayed DSB-mediated homologous pairing. Analysis of *Spo11*β isoform–specific transgenic mice revealed that late RAD51/DMC1 foci in the PAR are genetically distinct from both early PAR foci and global foci and that late PAR foci promote efficient X-Y pairing, recombination, and male fertility. Our findings uncover specific mechanisms that surmount the unique challenges of X-Y recombination.

Meiotic recombination, initiated by programmed double-strand breaks (DSBs), promotes homologous chromosome (homolog) pairing during prophase I (*1*). A subset of DSBs matures into crossovers that physically connect homologs so that they orient properly on the first meiotic spindle. Because sex chromosome recombination and pairing are restricted to the PAR (*2*), at least one DSB must form within this small region, and the homologous PAR must be located and engaged in recombination to lead to a crossover. Accordingly, the PAR in males exhibits high crossover frequency (*2*, *3*), but sex chromosomes also missegregate more frequently than autosomes (*4*). Nevertheless, X-Y nondisjunction is rare, which suggests that there are mechanisms that ensure successful X-Y recombination.

X-Y pairing is more challenging than autosomal pairing, as it cannot be mediated by multiple DNA interactions along the length of the chromosomes. We used fluorescence in situ hybridization (FISH) (*5*) to compare timing of meiotic X-Y and autosomal pairing in mice (Fig. 1). At leptonema, when DSBs begin to form and only short chromosome axis segments are present, PAR and autosomal FISH probes were mostly unpaired. By early to mid-zygonema, when axes elongate and homologs become juxtaposed, distal ends of chr 18 and 19 were paired in ~50% of nuclei; by late zygonema, these regions were paired in nearly all nuclei (Fig. 1B and fig. S1). In contrast, the X and Y PARs were rarely paired before pachynema (Fig. 1B); hence, X-Y pairing is delayed compared with that of autosomes.

DSBs precede and are required for efficient homolog pairing in mouse meiosis (*6*, *7*). Nucleus-wide ("global") foci of DSB markers RAD51/DMC1 peak in number at early to mid-zygonema (Fig. 2A) (*8*, *9*). Because stable X-Y pairing occurs late, we asked whether PAR DSB kinetics is also delayed (Fig. 2B and fig. S2). More than half of cells had no RAD51/DMC1 focus in the PAR before late zygonema (Fig. 2C), distinct from global patterns. Only when global foci were already declining did the majority of cells (~70%) display PAR foci (Fig. 2C and fig. S2*i*). We interpret the lack of PAR foci to indicate that DSBs have not yet formed. Thus, we propose that PAR DSB formation and/or turnover are under distinct temporal control. We cannot exclude the alternative possibility that PAR DSBs have formed but are cytologically undetectable, for example, because RAD51/DMC1 have not yet been loaded onto DSB ends or because foci have already turned over. In either case, DSB dynamics and/or processing differs on the PAR.

Most sites marked by PAR RAD51/DMC1 foci appeared incapable of mediating stable pairing before early pachynema (~70% of late zygotene

[1]Molecular Biology Program, Memorial Sloan-Kettering Cancer Center, New York, NY 10065, USA. [2]Developmental Biology Program, Memorial Sloan-Kettering Cancer Center, New York, NY 10065, USA. [3]Department of Public Health and Cell Biology, Section of Anatomy, University of Rome Tor Vergata, 00133 Rome, Italy. [4]Howard Hughes Medical Institute, Memorial Sloan-Kettering Cancer Center, New York, NY 10065, USA.

*Present address: Institute of Human Genetics, CNRS, 34090 Montpellier, France.

†To whom correspondence should be addressed. E-mail: m-jasin@ski.mskcc.org (M.J.); s-keeney@ski.mskcc.org (S.K.)

BIOCHEMISTRY
including biophysical chemistry & molecular biology

ARTICLE

pubs.acs.org/biochemistry

Mitsugumin 23 Forms a Massive Bowl-Shaped Assembly and Cation-Conducting Channel

Elisa Venturi,[†] Kazuhiro Mio,[‡] Miyuki Nishi,[§] Toshihiko Ogura,[‡] Toshio Moriya,[‡,∥] Samantha J. Pitt,[†] Kazutaka Okuda,[§] Sho Kakizawa,[§] Rebecca Sitsapesan,[*,†] Chikara Sato,[*,‡] and Hiroshi Takeshima[*,§]

[†]School of Physiology and Pharmacology, Bristol Heart Institute and Centre for Nanoscience and Quantum Information, University of Bristol, Bristol, United Kingdom

[‡]Biomedical Research Institute and Biomedicinal Information Research Center, National Institute of Advanced Industrial Science and Technology, Tsukuba, Japan

[§]Graduate School of Pharmaceutical Sciences, Kyoto University, Kyoto, Japan

[∥]Graduate School of Comprehensive Human Sciences, University of Tsukuba, Tsukuba, Japan

Supporting Information

ABSTRACT: Mitsugumin 23 (MG23) is a 23 kDa transmembrane protein localized to the sarcoplasmic/endoplasmic reticulum and nuclear membranes in a wide variety of cells. Although the characteristics imply the participation in a fundamental function in intracellular membrane systems, the physiological role of MG23 is unknown. Here we report the biochemical and biophysical characterization of MG23. Hydropathicity profile and limited proteolytic analysis proposed three transmembrane segments in the MG23 primary structure. Chemical cross-linking analysis suggested a homo-oligomeric assembly of MG23. Ultrastructural observations detected a large symmetrical particle as the predominant component and a small asymmetric assembly as the second major component in highly purified MG23 preparations. Single-particle three-dimensional reconstruction revealed that MG23 forms a large bowl-shaped complex equipped with a putative central pore, which is considered an assembly of the small asymmetric subunit. After reconstitution into planar phospholipid bilayers, purified MG23 behaved as a voltage-dependent, cation-conducting channel, permeable to both K^+ and Ca^{2+}. A feature of MG23 gating was that multiple channels always appeared to be gating together in the bilayer. Our observations suggest that the bowl-shaped MG23 can transiently assemble and disassemble. These building transitions may underlie the unusual channel gating behavior of MG23 and allow rapid cationic flux across intracellular membrane systems.

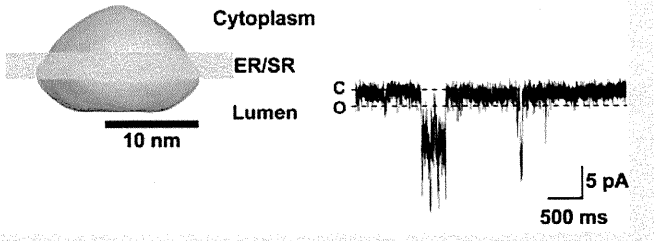

The endoplasmic/sarcoplasmic reticulum (ER/SR) is a multifunctional organelle responsible for important cellular processes, including protein maturation, lipid metabolism, Ca^{2+} signaling, and stress response. The ER/SR serves as an intracellular Ca^{2+} store, and activation of Ca^{2+} release channels, namely, inositol trisphosphate and ryanodine receptors, controls physiological functions such as muscle contraction, secretion, metabolism, and transcription.[1,2] In addition, the ER is the site for synthesis and maturation of both membrane and secretory proteins, enforcing protein glycosylation, disulfide bridging, folding, and subunit assembly. When misfolded proteins accumulate within the lumen, the ER stress response is activated according to severity, leading to the recruitment of ER chaperones, inhibition of protein synthesis, and induction of apoptotic cell death.[3,4] The activity of molecular chaperones, protein-processing enzymes, and metabolic enzymes of the ER largely depends upon the high luminal Ca^{2+} level.

Uptake of Ca^{2+} into and release of Ca^{2+} from intracellular stores are electrogenic processes. Therefore, active Ca^{2+} fluxes may be synchronized with the movements of other ionic species that compensate for charge imbalance across the ER/SR membrane.[5,6] We have recently identified TRIC channel subtypes that function as monovalent cation channels and probably support release of Ca^{2+} from the ER/SR of various cell types.[7−10] It is likely that the vital function of the ER/SR requires rapid and flexible control of the ionic balance between the luminal and cytoplasmic sides. To understand the ionic homeostasis across the ER/SR membrane, it is important to further characterize the functional properties of its constituent ion channels and transporters in the intracellular membrane system.

Skeletal and cardiac muscle SR is specialized as the intracellular Ca^{2+} store for controlling contraction and abundantly contains Ca^{2+}-handling proteins such as Ca^{2+}-ATPase, calsequestrin, and ryanodine receptors.[2] Muscle SR is, therefore, an ideal model system for studying Ca^{2+} store functions. To understand the molecular basis of Ca^{2+} stores, we have searched for novel SR proteins using monoclonal antibodies (mAbs) and previously identified mitsugumin 23 (MG23) with a mature

Received: December 7, 2010
Revised: February 15, 2011
Published: March 07, 2011

molecular size of 23 kDa.[11] Although MG23 is abundantly expressed in the SR and nuclear membranes of striated muscle cells, its expression is also detected in a wide variety of cell types. The ubiquitous distribution suggests that MG23 may contribute to a common function in intracellular membrane systems. A recent study demonstrated that mutant thymocytes lacking MG23 became resistant to DNA damage-induced apoptosis, suggesting a role in the generation of ER-derived cell death signals.[12] The physiological function of MG23, however, is still unknown. In this report, we provide biochemical and biophysical data suggesting that MG23 forms a massive homomultimeric complex, which can conduct cations, including Ca^{2+}, across the intracellular membrane systems.

MATERIALS AND METHODS

Antibody and Topology Analysis. For producing mAbs, two synthetic peptides corresponding to the N-terminal and C-terminal MG23 sequence were conjugated with a carrier protein and repeatedly injected into mice to generate hybridoma cells.[11] Immunochemical experiments established two clones, mAb7 (mAb-N) and mAb251 (mAb-C), which specifically recognize the corresponding antigen epitopes. To examine the transmembrane topology of MG23, we prepared SR vesicles from rabbit skeletal muscle[13] and isolated ER vesicles from HEK293 cells transfected with MG23 expression plasmids.[14] After the treatment of the vesicles with proteinase, the digestion profiles of native and recombinant MG23 were examined using mAbs as described previously.[15] For further details, see the Supporting Information.

Affinity Purification of Native and Recombinant MG23. For purification of native MG23, microsomal proteins were solubilized with NP-40 from rabbit muscle SR vesicles and reacted with affinity resin conjugated with mAb-N. After the resin had been extensively washed, MG23 was recovered with a buffer containing the epitope peptide. For production of recombinant MG23 using a methylotrophic yeast system (Invitrogen), a His tag sequence (Hisx6) was inserted into the rabbit MG23 cDNA at the site immediately downstream of the N-terminal signal sequence. The total microsome was prepared from yeast cells expressing His-tagged MG23, and the recombinant protein was solubilized with NP-40 or *n*-dodecyl β-D-maltoside (DDM) and purified using combined Ni and mAb-C affinity chromatography. For further details, see the Supporting Information. The purified MG23 preparations were used for chemical cross-linking, ultrastructural imaging, and channel recording.

Particle Image Analysis. After affinity purification, MG23 was further purified by density gradient centrifugation. For immunodecoration of MG23, mAbs were reacted with the purified preparations. MG23 particles with or without the mAb decoration were applied to thin carbon films, negatively stained, and examined using electron microscopy (EM). For three-dimensional (3D) reconstruction of MG23 structures,[7,16] particle images for the large bowl-shaped and asymmetric small structures were automatically picked up from the electron micrographs.[17,18] The particle images in each library were aligned rotationally and translationally[19−21] and classified into clusters.[22,23] The resulting class averages were used as new references, and the cycle from alignment to classification was repeated until convergence. On the basis of the symmetry of averaged images, 6-fold symmetry was imposed in the following computation of the large particles. No symmetry was assumed for the small particles. After convergence, a Euler angle was assigned to each average image,[24] and a primary 3D model was reconstructed using simultaneous iterative reconstruction techniques.[25] To optimize 3D reconstruction, reprojection images were created from the 3D model and used for realignment of the original particle images.[26] The aligned particles were classified again, and a Euler angle of each average was assigned so as to be the best correlation to the 3D reprojection image. The computational steps were repeated until a stable 3D model was obtained. For further details, see the Supporting Information.

Planar Phospholipid Bilayer Measurements. Native and recombinant MG23 proteins were solubilized and purified with either NP-40 or DDM. For detergent exchange in purified MG23 preparations, gel filtration chromatography was performed using a buffer solution containing 16 mM CHAPS and 16 mM 1,2-dimyristoyl-*sn*-glycero-3-phosphocholine (DMPC). Then, CHAPS was dialyzed using a dialysis membrane with a cutoff size of 12 kDa (Medicell International Ltd.) against a buffer containing 0.1 M NaCl, 0.1 mM EGTA, 25 mM PIPES (pH 7.4), 0.15 mM $CaCl_2$, and 2.5 mM DTT (exchanged every 4 h for 16 h). Purified native and recombinant MG23 proteins were fused with planar phosphatidylethanolamine lipid bilayers as previously described.[27] The *trans* chamber was held at ground and the *cis* chamber at potentials relative to ground. To examine if MG23 could behave as an ion channel permeable to monovalent cations or anions, we used symmetrical (in both *cis* and *trans* chambers) bathing solutions containing either 260 mM KCl, 20 mM HEPES, and 15 μM free Ca^{2+} (pH 7.2) or 260 mM K-PIPES and 15 μM free Ca^{2+} (pH 7.2). To investigate if MG23 is permeable to Ca^{2+}, we perfused the *cis* chamber with 250 mM HEPES, 80 mM Tris, and 15 μM free Ca^{2+} (pH 7.2) and filled the *trans* chamber with a solution containing 250 mM glutamic acid and 10 mM HEPES (pH 7.2) with $Ca(OH)_2$ (free Ca^{2+} concentration of 65 mM). The free Ca^{2+} concentration and pH of solutions were measured at 22 °C using a calcium electrode (Orion 93-20) and Ross-type pH electrode (Orion 81-55) as described previously.[27] Single-channel events were recorded on digital audiotape. MG23 recordings were filtered at 600 kHz (−3 dB) and digitized at 20 kHz using Pulse (HEKA, Elektronik Lambrecht/Pfalz). The amplitude of channel openings was determined using WinEDR version 3.05 (J. Dempster, University of Strathclyde, Glasgow, U.K.) using manually controlled cursors. Noise analysis was performed with WinEDR version 3.05. The current fluctuations across the bilayer were subdivided into multiple segments in time with each segment containing N samples. The mean current for each segment was calculated with the formula

$$I_{\text{mean}} = \frac{\sum_{i=1}^{N} I(i)}{N}$$

where $I(i)$ is the amplitude of the ith current of the N samples in the segment. The mean current values were then plotted versus time. The relative Ca^{2+}/K^+ permeability ratio ($P_{Ca^{2+}}/P_{K^+}$) of MG23 was calculated using the Fatt−Ginsborg equation:[28]

$$P_{Ca^{2+}}/P_{K^+} = [K^+]/4[Ca^{2+}] \exp(E_{rev}F/RT)[\exp(E_{rev}F/RT) + 1]$$

where R, T, and F have their usual meanings and E_{rev} is the zero-current reversal potential. The value of RT/F used was 25.4 mV at 22 °C. E_{rev} was determined under bi-ionic conditions (*cis*, 210 mM K^+; *trans*, 65 mM Ca^{2+}) and was taken as the voltage at

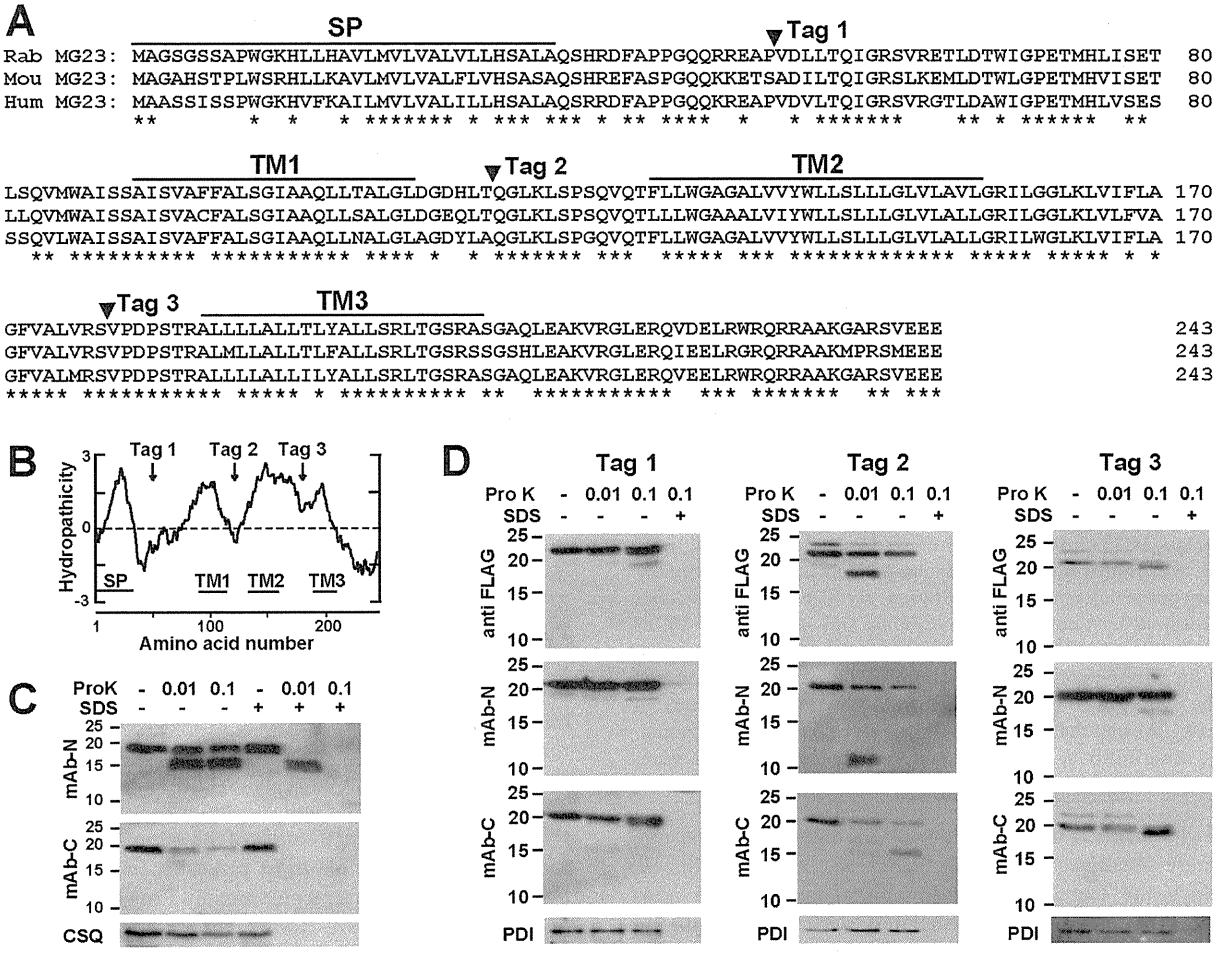

Figure 1. Membrane topology analysis of MG23. (A) Signal sequence (SP) and proposed transmembrane segments in MG23 aligned sequences. Amino acid residues are numbered from the initiating methionine, and sets of identical residues among the animal species are marked with asterisks. The sites inserted with a FLAG tag for the topology analysis are also indicated. Our topology analysis predicted three transmembrane segments (TM1–TM3); the termini of each segment are tentatively assigned. Rab, rabbit; Mou, mouse; Hum, human. (B) Hydropathicity profile of MG23. The hydropathicity was calculated using the Kyte–Doolittle algorithm with a window size of 19 residues. The N-terminal signal peptide (SP), putative transmembrane segments (TM1–TM3), and FLAG tag sites (Tag 1–3) are indicated. (C) Topology analysis of MG23 using skeletal muscle SR vesicles. The SR vesicles were treated with proteinase K at several concentrations (Pro K, micrograms per milliliter) in the presence or absence of 0.1% SDS. Proteolytic profiles were examined via Western blotting using mAb-N, mAb-C, or the antibody to calsequestrin (CSQ, SR luminal marker protein as a control). (D) Topology analysis of FLAG-tagged MG23 in ER vesicles. HEK293 cells were transfected with expression plasmids carrying FLAG-tagged MG23 cDNAs and harvested for the preparation of ER vesicles under isotonic conditions. The ER vesicles were treated with proteinase K in the presence or absence of SDS. Proteolytic profiles were examined via immunoblotting using mAb-N, mAb-C, mAb against the FLAG tag, or the antibody to protein disulfide isomerase (PDI, ER luminal marker protein). Size markers are indicated in kilodaltons.

which no current was detected. E_{rev} was corrected for the liquid junction potentials arising between the different solutions. The junction potential was calculated to be −3 mV using Clampex version 10.2 (Molecular Devices, Sunnyvale, CA).

RESULTS

Three Transmembrane Segments Proposed for MG23. After the N-terminal signal peptide of 33 amino acid residues is removed from the primary translational product (Figure 1A), mature MG23 is localized as a 23 kDa membrane protein in the skeletal muscle SR.[11] No mobility shift after the treatment of glycosidase and thiol-reducing agents in sodium dodecyl sulfate–polyacrylamide gel electrophoresis (SDS–PAGE) has suggested that mature MG23 is not subjected to obvious post-translational modifications such as glycosylation and disulfide linkage.[11] Although the Prosite database search detected no conserved motif sequences or domain structures, the hydropathicity profile suggests multiple membrane-spanning segments in MG23 (Figure 1B). First, we examined the transmembrane topology of MG23 in the muscle SR. MG23 was detected as a protein band with a relative molecular mass of ~19 kDa via SDS–PAGE. This band remained even after extensive digestion with proteinase K and was shown to be highly proteinase resistant in SR vesicles prepared under isotonic conditions. However, after proteinase treatments, we detected a cleaved product of ~16 kDa, which was recognized by mAb-N but not by mAb-C (Figure 1C). Therefore, the proteinase-insensitive N-terminus is assigned to the luminal side, and conversely, the proteinase-sensitive C-terminus probably faces into the cytoplasm.

We further introduced the FLAG tag sequence at hydrophilic sites in the MG23 primary structure and prepared ER vesicles from cultured cells expressing the FLAG-tagged MG23 proteins for proteolytic analysis (Figure 1D). The region around residue

dx.doi.org/10.1021/bi1019447 |*Biochemistry* 2011, 50, 2623–2632

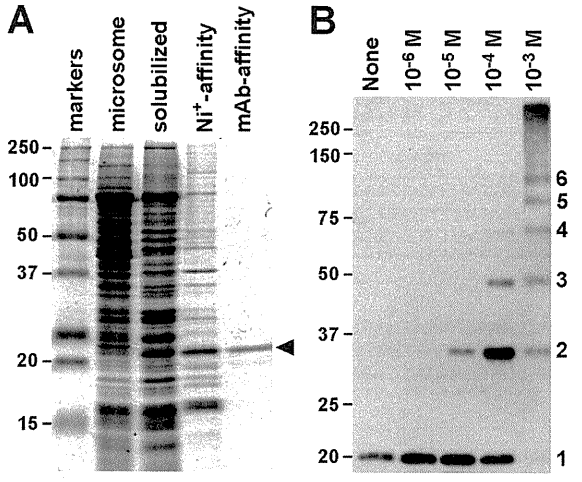

Figure 2. Purification and cross-linking of MG23. (A) Purification of recombinant MG23 from cDNA-transfected yeast cells. The cell lysate fraction, microsomal fraction, Ni affinity-purified fraction, and immunoaffinity-purified fraction were analyzed via SDS−PAGE. Proteins were visualized by Coomassie blue staining, and recombinant MG23 is marked with an arrowhead. (B) Cross-linking of purified recombinant MG23. An affinity-purified recombinant MG23 preparation was treated with the cross-linker disuccinimidyl glutarate at concentrations of 10^{-6}−10^{-3} M, and the resulting products were examined by immunoblotting using mAb-N; monomeric to hexameric products are numbered. Size markers are indicated in kilodaltons.

119 (Tag 2 site) was resistant to proteinase digestion but became proteinase-sensitive when the FLAG tag was introduced. Therefore, the Tag 2 site is reasonably assigned to the cytoplasmic side and may be associated with the membrane environment in the original form of mature MG23. On the other hand, no obvious difference in digestion pattern was observed by insertion of the tag at the Tag 1 and Tag 3 sites, suggesting their localization on the luminal side of the ER/SR. Taken together, the proteolytic analysis data predict three transmembrane segments, which are arranged in MG23 according to the positive-inside rule.[29] In this model (Figure 3C), of the 210 amino acid residues that composed the mature MG23, the cytoplasmic region contains 59 residues (28%), the transmembrane region carries 65 residues (31%), and the luminal region possesses 86 residues (41%).

Homo-Oligomeric Assembly of MG23. Native MG23 was solubilized from rabbit SR vesicles and purified using mAb affinity chromatography (Figure S1A of the Supporting Information). Although purified preparations contained a few impurities, including Ca^{2+}-ATPase (~100 kDa protein), no proteins were coenriched with MG23 during the affinity purification. Moreover, recombinant His-tagged MG23 was expressed in metanotrophic yeast (Figure 2A) and highly purified using combined affinity chromatography (>95% purity via SDS−PAGE). Both preparations were used to characterize the structural and electrophysiological properties of MG23 in this study. When native and recombinant MG23 preparations were reacted with chemical cross-linkers, immunoblotting detected the generation of homo-oligomeric products (Figure 2B). For example, cross-linking by disuccinimidyl glutarate generated oligomeric complexes, up to a hexamer, in both native and recombinant MG23 preparations (Figure S1B of the Supporting Information). The observations suggest that MG23 forms at least a homohexamer as a putative self-assembly unit.

MG23 Particle Imaging. After the negative staining, purified recombinant MG23 was examined by EM (Figure 3A). Most particles were round-shaped or bowl-shaped, which probably represent vertical or lateral views, respectively. We frequently detected round-shaped particles with electron-dense rim, interpreted to be the views of the MG23 particle perpendicular to the membrane. Putative side views clearly show asymmetry with respect to the membrane; one end is wider and the other narrower. To examine the topological orientation to the SR/ER membrane, recombinant MG23 particles were reacted with mAb to the N-terminal His tag (mAb-His) and mAb-C, and the resulting MG23−mAb complexes were analyzed by EM (Figure 3B). Although we frequently detected MG23 particles bearing multiple antibodies, mAb-His predominantly attached to the wider side of the particle, while mAb-C reacted with the narrower side. The EM observation, together with the proteolytic topology assay, suggests that the narrow side of the MG23 particle faces the cytoplasm while the wide side is oriented to the ER/SR lumen (Figure 3C).

3D Reconstruction of Bowl-Shaped MG23 Particles. To understand the molecular shape of MG23, we reconstructed its 3D structure by the single-particle reconstruction technique. Purified recombinant MG23 protein was adsorbed to the grid, blotted with the filter paper, negatively stained, and recorded by EM. MG23 particles were selected from the digitized films using our program, and a total of 11175 images were picked up for 3D reconstruction (Figure 4). The surface representation demonstrates that MG23 is a bowl-shaped molecule, 12 nm in height, 16 nm in side length, and 17 nm diagonally at the widest transmembrane region. Because of the symmetry of the averaged top view (Figure 4A, left-most panel, second row), we applied 6-fold symmetry in this reconstruction. Projection from the final density map (Figure 4A, row 4) compares well with the corresponding raw particle images (Figure 4A, row 1), indicating that our 3D reconstruction is consistent with the data set. The presumed position of the membrane is indicated by the transparent blue band in Figure 3C, so that the volume ratio across the membrane fits to the topology model based on the hydropathicity and protein chemical data. In height, the transmembrane region of the bowl-shaped structure is ~3 nm, the cytoplasmic domain extends ~5 nm, and the luminal domain extends ~4 nm. In the serial sections of this structure (Figure S2 of the Supporting Information), the thickness of the lateral wall is 28−35 Å in the transmembrane region. A plot of the Euler angles of 163 adopted class averages shows the nearly random orientation of MG23 on the grid surface (Figure S3A of the Supporting Information). According to the Fourier shell correlation (FSC) function, the resolution limit for the reconstruction is 2.0 nm by the correlation coefficient of 0.5 criterion (Figure S3B of the Supporting Information). The final reconstruction included 9172 particle images (82% of all the selected images).

3D Reconstruction of Smaller-Sized MG23 Particles. During the EM analysis described above, we realized that the recombinant MG23 preparations always contained considerable amounts of asymmetric particles that were relatively smaller than the bowl-shaped particle (Figure 3A). We also detected similar EM images showing the coexistence of the larger and smaller particles in native MG23 preparations purified from rabbit skeletal muscle (data not shown). Therefore, we also tried to reconstruct the 3D structure of the smaller-sized particles. A total of 1707 images of the smaller particles were collected from the digitized films and used for 3D reconstruction. Because no symmetry was observed in the averaged images or the raw

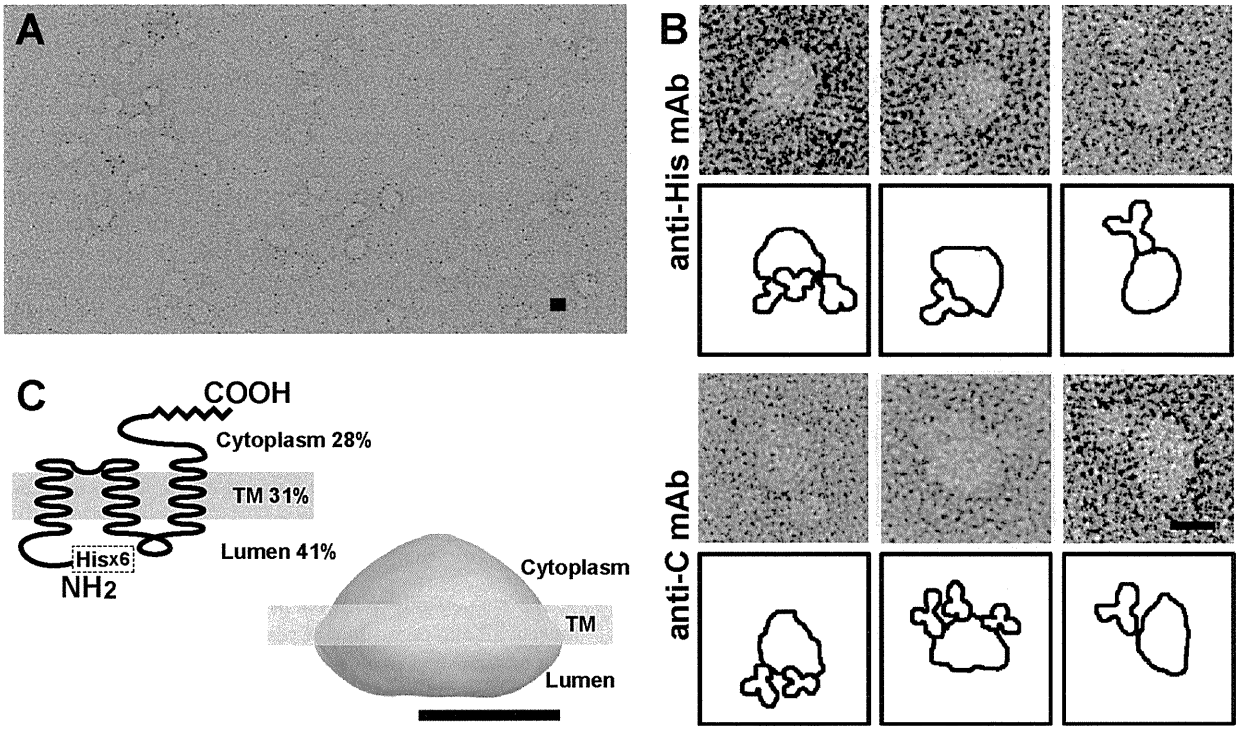

Figure 3. EM analysis of MG23 particles. (A) Raw EM images of recombinant MG23 particles. After adsorption to the glow-discharged carbon film, negatively stained samples were imaged by EM. (B) Immunodecoration of MG23 particles. Recombinant MG23 bearing anti-His mAbs (top panels) and mAb-C (bottom panels) were imaged by EM. (C) Predicted membrane topology of the MG23 monomer from the hydropathicity profile and limited proteolytic analysis (left) and the membrane position (blue line) deduced from the volume calculation of the reconstructed MG23 (right). Scale bars are 10 nm.

images, we reconstructed the smaller-sized molecule assuming no intramolecular symmetry. The surface representation demonstrates that the smaller asymmetric structure has a roughly crescent-shaped appearance, 14 nm in height, 11 nm in side length, and 6 nm in narrow side length (Figure 5). The almost random orientation of the particles on the grid surface was also shown by a plot of the Euler angles of the 117 adopted class averages (Figure S3C of the Supporting Information). According to the FSC function, the resolution limit for the smaller-sized structure is 3.6 nm by the correlation coefficient of 0.5 criterion (Figure S3D of the Supporting Information). The final reconstruction included 1699 particle images (99% of all the selected images).

Considering that the MG23 preparations were subjected to the EM analysis after affinity purification and size fractionation using sucrose gradient centrifugation, which were shown to be highly purified by SDS−PAGE, the concomitance of the large and small particles likely suggests that MG23 is easily disassembled and reassembled during purification and storage. We considered that the smaller particles constitute a partial domain of the bowl-shaped assembly (see Discussion and Figure S4 of the Supporting Information).

MG23 Conducts Cations. To investigate the possibility that MG23 plays a role in the transport of ions across the ER/SR, we reconstituted purified recombinant MG23 into planar lipid bilayers in symmetrical solutions of 260 mM KCl. Most incorporations into the bilayer consisted of the apparent insertion of multiple channels; however, on rare occasions, we observed what appeared to be opening events to a single consistent single-channel level. A representative experiment is shown in Figure 6A. The current−voltage relationship of these channel events (Figure 6B) yielded a conductance of 85.1 ± 5.3 pS ($n = 3$; mean ± standard deviation). A similar conductance of 88.2 ± 2.9 pS ($n = 5$) was observed in symmetrical solutions of 260 mM K-PIPES (Figure 6C), indicating that MG23 preferentially conducts cations.

MG23 is expressed in intracellular membranes, including the SR/ER Ca^{2+}-store membranes, and therefore, it is important to investigate if it is permeable to Ca^{2+}. To test this, we incorporated recombinant MG23 into bilayers using solutions that are typically used to monitor Ca^{2+} currents through ryanodine receptor channels:[27] 250 mM Tris/HEPES and 15 μM Ca^{2+} on the *cis* side and 65 mM Ca^{2+} on the *trans* side. Under these conditions, we observed single-channel current fluctuations indicating that Ca^{2+} is flowing in the *trans* to *cis* direction through MG23 (Figure 6D). No channel activity was observed in solutions of symmetrical 250 mM Tris/HEPES, demonstrating that the channel is not permeable to Tris or HEPES (Figure S5 of the Supporting Information). The current−voltage relationship in these Ca^{2+}-containing solutions exhibits a unitary conductance of 62.5 ± 10.2 pS ($n = 5$). Our observations therefore demonstrate that MG23 can form an ion channel that is permeable to both K^+ and Ca^{2+}. After incorporation of MG23 into bilayers, current−voltage relationships were obtained under bi-ionic conditions (*cis*, 210 mM K^+; *trans*, 65 mM Ca^{2+}). The reversal potential was calculated to be −6.9 ± −3.7 mV ($n = 3$) after correction for the junction potentials arising between the different solutions (Figure S6 of the Supporting Information). Using the Fatt−Ginsborg equation, the $P_{Ca^{2+}}/P_{K^+}$ for MG23 was then calculated as 1.1 ± 0.2 ($n = 3$), which suggests that MG23 is approximately equally permeable to Ca^{2+} and K^+.

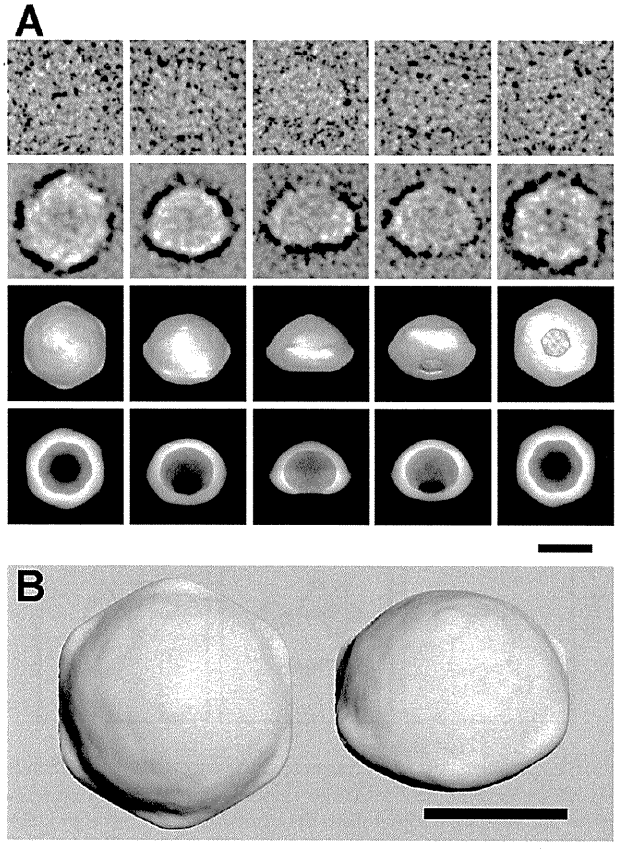

Figure 4. Reconstruction of the larger-sized MG23 particle. (A) First row, representative raw images; second row, corresponding class averages; third row, surface representations of the 3D reconstruction; fourth row, projections of the 3D reconstruction. Consistency among data sets is very high in size, shape, and inner structure, indicating successful 3D reconstruction from the original images of recombinant MG23 particles. (B) Surface representation of two MG23 structures from top (left) and oblique (right) views. Dimensions of the larger-sized bowl-shaped structure are 12 nm (height), 16 nm (wide side length), and 17 nm (diagonally at the widest transmembrane region). The scale bars are 10 nm.

Distinctive Characteristics and Voltage Dependence of MG23 Channel Gating. In the majority of experiments with MG23 preparations, multiple active channels were observed in the bilayer. This occurred even when we saw what appeared to be single fusion events of the liposomes into the bilayer. The presence of multiple channels and the frequent brief open events usually produced "messy-looking" or "flickery" single-channel recordings. Another distinctive characteristic of MG23 gating was the fact that multiple channels appeared to gate in unison so that many channels opened and closed together in a coupled or coordinated manner. Both the flickery gating and the coordinated channel openings can be seen in the two types of experiments: one in which K^+ is the permeant ion (Figure 7A) and another in which Ca^{2+} is the permeant ion (Figure 7B). In both channel measurements, we observed single opening events (asterisks), coordinated gating of multiple channels (arrowheads), and long sojourns of coordinated gating (bar). We have not identified any tendency for a preferred number of MG23 channels to gate together in synchrony; this seems to be a random process. For example, two channels may open and close together (as in Figure 7B), or greater numbers of channels may gate in a synchronous fashion.

Because coordinated gating of multiple channels occurred randomly and gating was usually very rapid giving rise to flickering events, it was very difficult to measure the single-channel open probability (P_o) of MG23 channels. To examine the voltage dependence of MG23 channel gating, we therefore used noise analysis (see Figure 7C for a typical example). At 10 mV (channel openings are downward deflections), P_o was fairly low, although there were several coordinated channel opening events. At −10 mV (channel openings are upward deflections), there were more channel openings, and at −20 mV, the channels became very active and it was obvious that there were many channels present in the bilayer. The strong voltage dependence of MG23 is an important distinguishing feature of this channel and was observed in every experiment. Typically, channel activity was low around 0 mV but rapidly increased as the holding potential was made more negative. Holding potentials above −30 mV tended to break the bilayer because of the large currents.

DISCUSSION

We successfully purified MG23 proteins from both rabbit muscle SR and recombinant yeast using affinity chromatography. The original EM images of the MG23 preparations themselves clearly suggested that the predominant large particles are morphologically identical in native and recombinant MG23 preparations. However, even after the size fractionation of highly purified MG23 by sucrose gradient centrifugation, MG23 particles were not uniform in size. In the MG23 preparations, the predominant component was the bowl-shaped particle with 6-fold symmetry (Figure 4), but we also detected the smaller crescent-shaped particles as the second most common component (Figure 5). The application of chemical cross-linkers to MG23 preparations reproducibly generated the homohexamer as a putative basic self-assembly unit (Figure 2). However, it is unlikely that these larger and smaller structures observed using EM represent hexameric and monomeric MG23, respectively. This is because the MG23 monomer at 23 kDa, composed of 210 amino acids, is too small for EM observation (for reference, see the images of 150 kDa mAbs in Figure 3B). We therefore propose that the crescent-shaped particle is a hexameric minimum structural subunit of MG23, and that multiple subunits subsequently constitute a larger assembly such as the bowl-shaped structure. With the available data, we could not determine the exact number of crescent-shaped subunits that would make up the full particle, but biochemical and structural analysis points to a number composed of two to six subunits. Fitting of more than six crescent-shaped subunits to the bowl-shaped structure seemed impossible. We present a docking of six crescent-shaped subunits as the most plausible model (Figure S4 of the Supporting Information). The 3D map of the crescent-shaped subunit (Figure 5B) is contoured at an isosurface containing a volume corresponding to 138 kDa (23 kDa × 6), and the bowl-shaped particle (Figure 4B) at 828 kDa (138 kDa × 6) using Imagic V,[19] assuming a hexagonal assembly of the crescent-shaped subunit. However, this simulation could not exclude other possibilities of subunit construction in the bowl-shaped particle.

MG23 is expressed in various cell types and localized in the SR/ER and nuclear membranes.[11] Our bilayer experiments demonstrate that recombinant MG23 prepared using DDM or NP-40 as a detergent forms cation channels displaying little difference in permeability between K^+ and Ca^{2+}. MG23 gating behavior is very unusual; the simultaneous openings (and therefore apparent

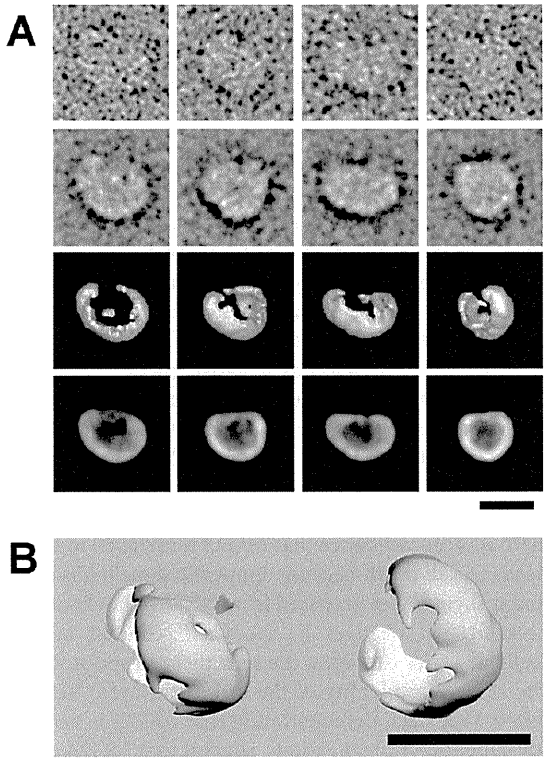

Figure 5. Reconstruction of the smaller-sized MG23 particle. (A) First row, representative raw images; second row, corresponding class averages; third row, surface representations; fourth row, projections of the 3D reconstruction. (B) Dimensions of the smaller-sized crescent-shaped molecule are 14 nm (height), 11 nm (wide side length), and 6 nm (narrow side length). The massive bowl-shaped particle in Figure 3 is considered to be an assembly of multiples of this small subunit. The scale bars are 10 nm.

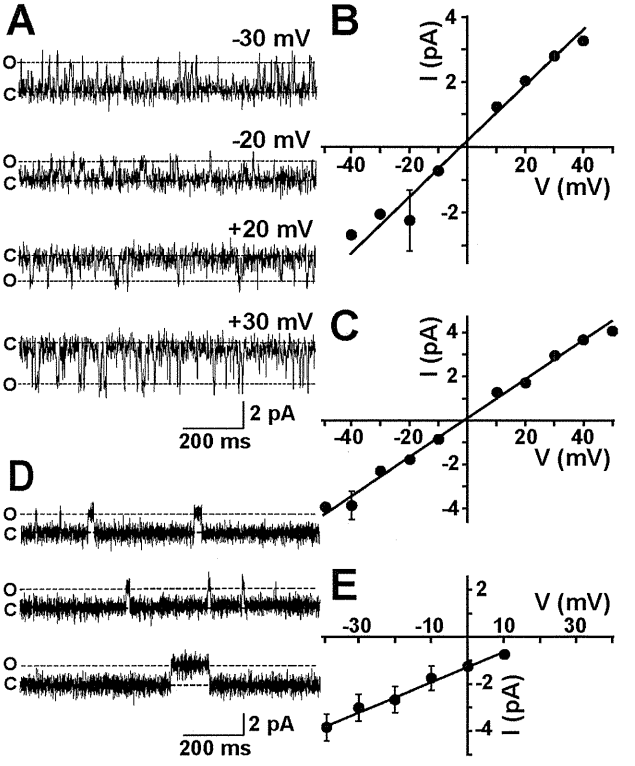

Figure 6. Single-channel behavior of MG23. (A) Representative single-channel recordings of native MG23 from rabbit skeletal muscle in solutions of symmetrical 260 mM KCl and 20 mM HEPES (pH 7.2). The holding potentials are indicated, and O and C represent the open and closed channel levels, respectively. (B) Single-channel current–voltage relationship of recombinant MG23 in symmetrical 260 mM KCl solutions (n = 3). (C) Single-channel current–voltage relationship of recombinant MG23 in symmetrical 260 mM K-PIPES solutions (n = 5). (D) Channel gating of recombinant MG23 with Ca^{2+} as the permeant ion. The bathing solutions contained 250 mM HEPES, 80 mM Tris (pH 7.2), and 15 μM free Ca^{2+} in the *cis* chamber and 250 mM glutamic acid and 10 mM HEPES (pH 7.2) with $Ca(OH)_2$ (free Ca^{2+} concentration of 65 mM) in the *trans* chamber. The holding potential was 0 mV. Channel openings at holding potentials more positive than 10 mV could not be resolved. (E) Current–voltage relationship of MG23 under the conditions described in panel D (n = 5). The data represent means ± the standard deviation.

coordination) of seemingly random numbers of MG23 channels were a consistent feature of the gating of this channel (Figure 7). As described above, particle image analysis implies that the crescent-shaped subunits are unstably assembled into the bowl-shaped particle that is equipped with a putative central pore. Although we can only speculate about how MG23 conducts ions, the unusual gating features could be caused by the proposed instability of the bowl-shaped particle. For example, MG23 may operate as a single conduction pathway with a central pore in the bowl-shaped assembly. During the disintegration and re-formation of the assembly, the proposed channel pore might display multiple conductance states and could pass huge currents superficially observed as simultaneous gating events. Alternatively, it may be possible that the crescent-shaped subunits form the unitary ion channel and can gate independently in the bilayer. In response to the structural transitions of the bowl-shaped assembly, the resulting conformational changes might affect ionic conduction through each crescent-shaped channel or could induce the simultaneous openings of the multiple-channel components. On the basis of our reconstructed 3D particle images, it is not possible to locate the ion conduction pathway of the MG23 channel. However, if MG23 is to follow the structural conventions of ion channels with known X-ray crystal structures, the apparent thickness at the transmembrane region of the crescent-shaped subunit (Figure S2 of the Supporting Information) suggests that it may be too narrow to form a unitary conduction pathway, hence favoring the idea of a single central pore in the bowl-shaped particle.

A novel ER/SR cation channel such as MG23, exhibiting no obvious selectivity for monovalent over divalent cations, would be expected to contribute significantly to the regulation of cellular Ca^{2+} homeostasis. There are many aspects of intracellular Ca^{2+} release that are not fully understood, and characterizing the biophysical properties of SR proteins such as MG23 will be important in resolving these issues. For example, electrogenic release of Ca^{2+} from and reuptake of Ca^{2+} into the ER/SR require synchronized counterion movements to balance the buildup of charge asymmetry across the ER/SR membrane,[5,6,30,31] yet the molecular machinery responsible for the proposed counterion fluxes remains undefined. MG23 could play some part in that process. The purified MG23 channel displays a consistent voltage dependence of activation, indicating that it incorporates into the bilayer in a fixed orientation. SR vesicles also form in a fixed orientation[13] and are incorporated into artificial membranes in a fixed orientation such that the cytosolic side of SR ion channels always faces into the *cis* chamber.[32] Because our biochemical data (Figures 1–4) indicate that purified

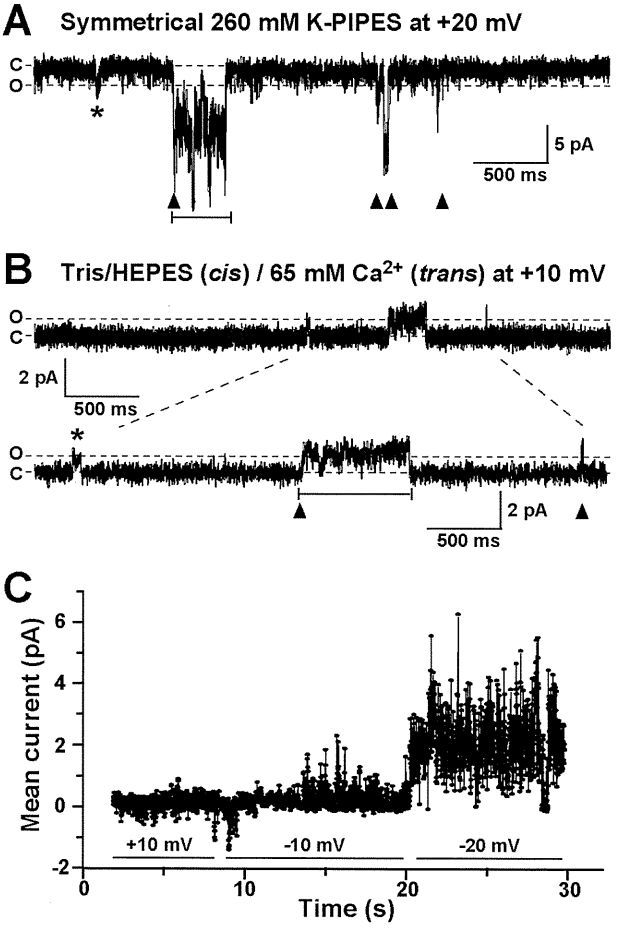

Figure 7. Distinguishing gating characteristics of MG23. (A) Coordinated gating of recombinant MG23 channels in symmetrical solutions of 260 mM K-PIPES (pH7.2) at a holding potential of 20 mV. C indicates the zero current level (all channels closed), and O indicates the current level of a single MG23 channel opening; the dashed lines aid the visualization of these levels across the trace. An asterisk denotes a single MG23 channel opening. The arrowheads indicate where coordinated gating of multiple MG23 channels occurs, and the bar shows a long coordinated gating event. (B) Typical example of the coordinated MG23 channel gating in solutions where *trans* Ca^{2+} was the only permeant ion (250 mM Tris/HEPES, *cis*; 65 mM Ca^{2+}, *trans*) at a holding potential of 10 mV. The dashed lines between the top and bottom traces indicate the portion of the trace that has been reproduced below on an expanded time scale to visualize the individual channel openings more clearly. (C) Noise analysis illustrates the voltage dependence of MG23 channels in symmetrical solutions of 260 mM K-PIPES (pH 7.2). As the holding potential became increasingly negative, K^+ current across the bilayer became more elevated.

MG23, when reconstituted into liposomes, retains the same orientation as native MG23 in SR vesicles, it is most probable that the cytosolic side also faces into the *cis* chamber. Thus, in a cellular environment, given the voltage dependence of MG23 (Figure 7), it would be expected that during a Ca^{2+} release event, the ER/SR would become negative relative to the cytosol and this would reduce the P_o of the MG23 channel, although it would not close completely. If voltage was the only controlling influence on P_o, MG23 would tend to be more open during refilling of the ER/SR stores or just before a Ca^{2+} release event. MG23 may therefore contribute to the spontaneous Ca^{2+} leak that is known to occur from intracellular stores in many cell types.[33−35] In cardiac cells, this is termed diastolic SR Ca^{2+} leak, and there is growing evidence that this is increased in disease states such as heart failure and leads to an increased likelihood of fatal cardiac arrhythmias.[35−37] Indeed, in cardiac cells, it has been suggested that there must be another route for the release of Ca^{2+} from the SR during diastole apart from ryanodine receptors;[38] further investigation is required to determine whether MG23 is that pathway. On the other hand, the voltage dependence and sporadic gating behavior of MG23 suggest that it may play a more minor role in balancing charge asymmetry during a large and rapid Ca^{2+} release event (such as during a cardiac Ca^{2+} transient) than the recently characterized TRIC channels that are activated to high Po values as negative charge develops in the SR.[9] The full magnitude of MG23's contribution to counterion currents, however, will not be realized until we have an improved understanding of whether the function of MG23 can be regulated by soluble ligands or by other mechanisms such as phosphorylation and nitrosylation.

There is recent evidence that MG23 is involved in the process that leads to cell death because apoptotic signaling is attenuated in mutant thymocytes prepared from MG23-knockout mice.[12] It is accepted that changes in the Ca^{2+} content and leak of intracellular stores can affect the sensitivity to apoptotic death,[39] but the molecular identity of the leak pathway(s) has not been identified. Our data, demonstrating that MG23 is permeable to monovalent and divalent cations, suggest that MG23 could fulfill that role. It is clear that much work is required to link the unique structural features of MG23 to its equally unique behavior as an ion channel. For example, does the transient assembly or breakdown of the bowl-shaped MG23 particle underlie the sporadic activity of multiple MG23 channels opening simultaneously, or does the production of MG23 bowls and their appearance in the ER membrane lead to the destruction of ionic gradients across the ER and immediate cell death? What is the role of MG23 in nuclear membranes because it is clearly present there in high levels? Again, to answer this question, we require a much more detailed understanding of the ion conducting properties of MG23 and of how MG23 channel gating can be regulated. Investigating the phenotype of the knockout mouse will also be vital in identifying the key physiological and pathophysiological roles of the MG23 protein.

■ ASSOCIATED CONTENT

Supporting Information. Detailed methodology (Supporting Experimental Procedures), purification and cross-linking of native MG23 (Figure S1), continuous sections through the bowl-shaped MG23 particle (Figure S2), Euler angle distribution and FSC function in the 3D reconstruction of MG23 particles (Figure S3), docking model of the crescent-shaped subunits into the bowl-shaped particle (Figure S4), MG23 is not permeable to Tris and HEPES (Figure S5), and MG23 $P_{Ca^{2+}}/P_{K^+}$ data (Figure S6). This material is available free of charge via the Internet at http://pubs.acs.org.

■ AUTHOR INFORMATION

Corresponding Author

*H.T.: Graduate School of Pharmaceutical Sciences, Kyoto University, Kyoto 606-8501, Japan; telephone, +81-75-753-4572; fax, +81-75-753-4605; e-mail, takeshim@pharm.kyoto-u.ac.jp. C.S.: Biomedical Research Institute and Biomedicinal

Information Research Center, National Institute of Advanced Industrial Science and Technology, Ibaragi 305-8566, Japan; telephone, +81-298-61-5562; fax, +81-298-61-6478; e-mail, ti-sato@aist.go.jp. R.S.: School of Physiology and Pharmacology, Bristol Heart Institute and Centre for Nanoscience and Quantum Information, University of Bristol, Bristol BS8 1TD, United Kingdom; telephone, +44-117-331-1450; fax, +41-117-331-2288; e-mail, R.Sitsapesan@bristol.ac.uk.

Author Contributions

E.V., K.M., and M.N. contributed equally to this work.

Funding Sources

This work was supported in part by research grants from the Japan Society for the Promotion of Science, the Ministry of Education, Culture, Sports, Science and Technology, the Japan New Energy and Industrial Technology Development Organization, the British Heart Foundation, the Astellas Foundation, the Mochida Memorial Foundation, the Kanae Foundation, the Daiichi-Sankyo Foundation of Life Science, and the Takeda Science Foundation.

■ ACKNOWLEDGMENT

We thank S. Aoki and M. Mio for technical assistance.

■ ABBREVIATIONS

3D, three-dimensional; DDM, *n*-dodecyl β-D-maltoside; ER, endoplasmic reticulum; EM, electron microscopy; FSC, Fourier shell correlation; mAb, monoclonal antibody; MG23, mitsugumin 23; SR, sarcoplasmic reticulum

■ REFERENCES

(1) Berridge, M. J. (2002) The endoplasmic reticulum: A multifunctional signaling organelle. *Cell Calcium 32*, 235–249.

(2) MacLennan, D. H., Abu-Abed, M., and Kang, C.-H. (2002) Structure-function relationships in Ca^{2+} cycling proteins. *J. Mol. Cell. Cardiol. 34*, 897–918.

(3) Ron, D., and Walter, P. (2007) Signal integration in the endoplasmic reticulum unfolded protein respose. *Nat. Rev. Mol. Cell Biol. 8*, 519–529.

(4) Kim, I., Xu, W., and Reed, J. C. (2008) Cell death and endoplasmic reticulum stress: Disease relevance and therapeutic opportunity. *Nat. Rev. Drug Discovery 7*, 1013–1030.

(5) Meissner, G. (1983) Monovalent ion and calcium ion fluxes in sarcoplasmic reticulum. *Mol. Cell. Biochem. 55*, 65–82.

(6) Floyd, R., and Wray, S. (2007) Calcium transporters and signalling in smooth muscle. *Cell Calcium 42*, 467–476.

(7) Yazawa, M., Ferrante, C., Feng, J., Mio, K., Ogura, T., Zhang, M., Lin, P.-H., Pan, Z., Komazaki, S., Kato, K., Nishi, M., Zhao, X., Weisleder, N., Sato, C., Ma, J., and Takeshima, H. (2007) TRIC channels are essential for Ca^{2+} handling in intracellular stores. *Nature 448*, 78–82.

(8) Yamazaki, D., Komazaki, S., Nakanishi, H., Mishima, A., Nishi, M., Yazawa, M., Yamazaki, T., Taguchi, R., and Takeshima, H. (2009) Essential role of TRIC-B channel in Ca^{2+}-handling of alveolar epithelium and perinatal lung maturation. *Development 136*, 2355–2361.

(9) Pitt, S. J., Park, K.-H., Nishi, M., Urashima, T., Aoki, S., Yamazaki, D., Ma, J., Takeshima, H., and Sitsapesan, R. (2010) Charade of the SR K^+-channel: Two ion-channels, TRIC-A and TRIC-B, masquerade as a single K^+-channel. *Biophys. J. 99*, 417–426.

(10) Zhao, X., Yamazaki, D., Park, K.-H., Komazaki, S., Tjondrokoesoemo, A., Nishi, M., Lin, P., Hirata, Y., Brotto, M., Takeshima, H., and Ma, J. (2010) Ca^{2+} overload and sarcoplasmic reticulum instability in tric-a null skeletal muscle. *J. Biol. Chem. 285*, 37370–37376.

(11) Nishi, M., Komazaki, S., Iino, M., Kangawa, K., and Takeshima, H. (1998) Mitsugumin 23, a novel transmembrane protein on endoplasmic reticulum and nuclear membranes. *FEBS Lett. 432*, 191–196.

(12) Yamazaki, T., Sasaki, N., Nishi, M., and Takeshima, H. (2010) Facilitation of DNA damage-induced apoptosis by endoplasmic reticulum protein mitsugumin 23. *Biochem. Biophys. Res. Commun. 392*, 196–200.

(13) Saito, A., Seiler, S., Chu, A., and Fleischer, S. (1984) Preparation and morphology of sarcoplasmic reticulum terminal cisterae from rabbit skeletal muscle. *J. Cell Biol. 99*, 875–885.

(14) Zhang, M., Yamazaki, T., Yazawa, M., Treves, S., Nishi, M., Murai, M., Shibata, E., Zorzato, F., and Takeshima, H. (2007) Calumin, a novel Ca^{2+}-binding transmembrane protein on the endoplasmic reticulum. *Cell Calcium 42*, 83–90.

(15) Feramisco, J. D., Goldstein, J. L., and Brown, M. S. (2004) Membrane topology of human insig-1, a protein regulator of lipid synthesis. *J. Biol. Chem. 279*, 8487–8496.

(16) Mio, K., Ogura, T., Kiyonaka, S., Hiroaki, Y., Tanimura, Y., Fujiyoshi, Y., Mori, Y., and Sato, C. (2007) The TRPC3 channel has a large internal chamber surrounded by signal sensing antennas. *J. Membr. Biol. 367*, 373–383.

(17) Ogura, T., and Sato, C. (2004) Automatic particle pickup method using a neural network has high accuracy by applying an initial weight derived from eigenimages: A new reference free method for single-particle analysis. *J. Struct. Biol. 145*, 63–75.

(18) Ogura, T., and Sato, C. (2004) Auto-accumulation method using simulated annealing enables fully automatic particle pickup completely free from a matching template or learning data. *J. Struct. Biol. 146*, 344–358.

(19) van Heel, M., Gowen, B., Matadeen, R., Orlova, E. V., Finn, R., Pape, T., Cohen, D., Stark, H., Schmidt, R., Schatz, M., and Patwardhan, A. (2000) Single-particle cryo-electron microscopy: Towards atomic resolution. *Q. Rev. Biophys. 33*, 307–369.

(20) Frank, J. (2006) *Three-dimensional electron microscopy of macromolecular assembles: Visualization of biological molecules in their native state*, Oxford University Press, New York.

(21) Harauz, G., and van Heel, M. (1986) Exact filters for general geometry 3-dimensional reconstruction. *Optik 73*, 146–156.

(22) Ogura, T., Iwasaki, K., and Sato, C. (2003) Topology representing network enables highly accurate classification of protein images taken by cryo-electron-microscope without masking. *J. Struct. Biol. 143*, 185–200.

(23) Bretaudiere, J. P., and Frank, J. (1986) Reconstitution of molecule images analysed by correspondence analysis, a tool for structural interpretation. *J. Microsc. (Oxford, U.K.) 144*, 1–14.

(24) Ogura, T., and Sato, C. (2006) A fully automatic 3D reconstruction method using simulated annealing enables accurate posterioric angular assignment of protein projections. *J. Struct. Biol. 158*, 371–386.

(25) Penczek, P., Radermacher, M., and Frank, J. (1992) Three-dimensional reconstruction of single particles embedded in ice. *Ultramicroscopy 40*, 33–53.

(26) Penczek, P. A., Grassucci, R. A., and Frank, J. (1994) The ribosome at improved resolution: New techniques for merging and orientation refinement in 3D cryo-electron microscopy of biological particles. *Ultramicroscopy 53*, 251–270.

(27) Sitsapesan, R., Montgomery, R. A., MacLeod, K. T., and Williams, A. J. (1991) Sheep cardiac sarcoplasmic reticulum calcium-release channels: Modification of conductance and gating by temperature. *J. Physiol. 434*, 469–488.

(28) Fatt, P., and Ginsborg, B. L. (1958) The ionic requirements for the production of action potentials in crustacean muscle fibres. *J. Physiol. 142*, 516–543.

(29) von Heijne, G. (1992) Membrane protein structure prediction. Hydrophobicity analysis and the positive-inside rule. *J. Mol. Biol. 225*, 487–494.

(30) Somlyo, A. P., and Somlyo, A. V. (1986) Electron probe analysis of calcium content and movements in sarcoplasmic reticulum, endoplasmic reticulum, mitochondria, and cytoplasm. *J. Cardiovasc. Pharmacol. 8*, S42–S47.

(31) Somlyo, A. P., Somlyo, A. V., Shuman, H., and Endo, M. (1982) Calcium and monovalent ions in smooth muscle. *Fed. Proc. 41*, 2883–2890.

(32) Sitsapesan, R., and Williams, A. J. (1994) Gating of the native and purified cardiac SR Ca^{2+}-release channel with monovalent cations as permeant species. *Biophys. J. 67*, 1484–1494.

(33) Giunti, R., Gamberucci, A., Fulceri, R., Bánhegyi, G., and Benedetti, A. (2007) Both translocon and a cation channel are involved in the passive Ca^{2+} leak from the endoplasmic reticulum: A mechanistic study on rat liver microsomes. *Arch. Biochem. Biophys. 462*, 115–121.

(34) Lomax, R. B., Camello, C., van Coppenolle, F., Petersen, O. H., and Tepikin, A. V. (2002) Basal and physiological Ca^{2+} leak from the endoplasmic reticulum of pancreatic acinar cells. Second messenger-activated channels and translocons. *J. Biol. Chem. 277*, 26479–26485.

(35) Eisner, D. A., Kashimura, T., O'Neill, S. C., Venetucci, L. A., and Trafford, A. W. (2009) What role does modulation of the ryanodine receptor play in cardiac inotropy and arrhythmogenesis? *J. Mol. Cell. Cardiol. 46*, 474–481.

(36) Wehrens, X. H., Lehnart, S. E., and Marks, A. R. (2005) Intracellular calcium release and cardiac disease. *Annu. Rev. Physiol. 67*, 69–98.

(37) Benkusky, N. A., Farrell, E. F., and Valdivia, H. H. (2004) Ryanodine receptor channelopathies. *Biochem. Biophys. Res. Commun. 322*, 1280–1285.

(38) Santiago, D. J., Curran, J. W., Bers, D. M., Lederer, W. J., Stern, M. D., Ríos, E., and Shannon, T. R. (2010) Ca sparks do not explain all ryanodine receptor-mediated SR Ca leak in mouse ventricular myocytes. *Biophys. J. 98*, 2111–2120.

(39) Pinton, P., Giorgi, C., Siviero, R., Zecchini, E., and Rizzuto, R. (2008) Calcium and apoptosis: ER-mitochondria Ca^{2+} transfer in the control of apoptosis. *Oncogene 27*, 6407–6418.

Heart Vessels (2010) 25:556–564
DOI 10.1007/s00380-010-0008-1

ORIGINAL ARTICLE

The role of the large-conductance voltage-dependent and calcium-activated potassium (BK_{Ca}) channels in the regulation of rat ductus arteriosus tone

Fang Sun · Emiko Hayama · Yasuhiro Katsube · Rumiko Matsuoka · Toshio Nakanishi

Received: 13 April 2009 / Accepted: 10 December 2009 / Published online: 9 October 2010

Abstract The role of large-conductance voltage-dependent and calcium-activated potassium (BK_{Ca}) channels in the regulation of ductus arteriosus (DA) tone is not clear. This study aimed to examine whether BK_{Ca} α and β subunits and BK_{Ca} currents are present in the rat DA, as well as whether the BK_{Ca} channels are involved in O_2-induced ductal constriction. BK_{Ca} α and β subunit transcripts (mRNAs) were detected in the DA from premature (19D) and mature (21D) rat fetuses and full-term neonates (NB) by quantitative real-time PCR. The amount of BK_{Ca} α mRNAs decreased with advancing development. $\beta 1$ was the dominant β subunit in the DA, and the amount of $\beta 1$ mRNAs was greatest in the mature DA. Immunofluorescence staining showed that the majority of BK_{Ca} α and $\beta 1$ proteins were colocated with alpha smooth muscle actin (α-SMA) in the tunica media of the DA in all age groups. The protein expression of the α subunit was greatest in the mature DA, while the expression of the $\beta 1$ subunit did not differ among all three groups. The 19D and 21D ductus tensions were recorded under various conditions by myograph. The 19D ductus rings exhibited poor O_2 sensitivity and no response to BK_{Ca} inhibitor (paxilline) or activator (NS1619). The 21D ductus rings developed significant constriction induced by O_2. Paxilline did not increase the 21D DA tension under either hypoxic or oxygenated conditions. NS1619 dilated the 21D DA only under oxygenated conditions. The recorded BK_{Ca} currents were greatest in the 21D DA smooth muscle cells (SMCs) upon using a whole-cell patch clamp. Our study indicated that BK_{Ca} channels exist in the DA but are not involved in O_2-induced ductal constriction. Activation of BK_{Ca} channels led to vasodilatation in the preconstricted DA induced by O_2, possibly suggesting a way to maintain the patency of DA after birth.

Keywords Ductus arteriosus · BK_{Ca} channel · O_2-induced ductal constriction

Abbreviations

DA	Ductus arteriosus
BK_{Ca}	Large-conductance voltage-dependent and calcium-activated potassium
SMC	Smooth muscle cell
19D	19 days of gestation
21D	21 days of gestation
NB	Newborn
α-SMA	Alpha smooth muscle actin
NS1619	13-Dihydro-1-[2-hydroxy-5-(trifluoromethyl)phenyl]-5-(trifluoromethyl)-2H-benzimidazol-2-one

F. Sun · E. Hayama · R. Matsuoka · T. Nakanishi
International Research and Educational Institute for Integrated Medical Sciences, Tokyo Women's Medical University, 8-1 Kawada-cho, Shinjuku-ku, Tokyo 162-8666, Japan

F. Sun
Division of Integrated Medical Sciences, Institute of Advanced Biomedical Engineering and Science, Graduate School of Medicine, Tokyo Women's Medical University, 8-1 Kawada-cho, Shinjuku-ku, Tokyo 162-8666, Japan

Y. Katsube
Department of Pediatrics, Nippon Medical School Musashikosugi Hospital, 1-396 Kosugi-cho, Nakahara-ku, Kawasaki, Kanagawa 211-8533, Japan

T. Nakanishi (✉)
Department of Pediatric Cardiology, Tokyo Women's Medical University, 8-1 Kawada-cho, Shinjuku-ku, Tokyo 162-8666, Japan
e-mail: pnakanis@hij.twmu.ac.jp

Introduction

The ductus arteriosus (DA) is a pivotal shunt in fetal life that connects the main pulmonary artery to the descending aorta to allow blood to bypass the unexpanded lungs. Closure of the DA after birth is a necessary step for normal transition from fetal to neonatal circulation. After birth, an increase in O_2 tension (PO_2) and a decrease in prostaglandin E2 production normally cause DA constriction [1].

The responses of the DA to changes in PO_2 vary depending on the developmental stage, increasing as development progresses [1, 2]. The abrupt increase in PO_2 at birth is clearly an initiating mechanism for functional ductal closure, and is followed by a slower process of anatomic obliteration [3–5]. The precise mechanisms of the O_2-induced ductal constriction remain unclear [1, 2]. It is known that membrane depolarization of DA smooth muscle cells (SMCs) occurs with the elevation of PO_2 from about −60 mV (resting potential) to −20 mV [6]. Potassium channels regulate membrane potential and hence vascular tone. The closure of potassium channels results in membrane depolarization, an increase in Ca^{2+} influx via voltage-dependent calcium channels, and vasoconstriction. Conversely, the activation of potassium channels induces vasodilation. The major potassium channels expressed in the vasculature include ATP-sensitive potassium (K_{ATP}) channels, voltage-dependent potassium (K_V) channels, and calcium-activated potassium (K_{Ca}) channels [7]. Nakanishi et al. [3] was the first to report that O_2 caused ductal constriction by closing K_{ATP} channels, which in turn increases Ca^{2+} influx via L-type voltage-dependent calcium channels. Tristani-Firouzi et al. [4] later reported that K_V channels are involved in the constrictor response of the DA to O_2. The role of K_{Ca} channels in O_2-induced ductal constriction remains unclear. The K_{Ca} channel family consists of a small-conductance group (SK_{Ca}), an intermediate-conductance group (IK_{Ca}) and a large-conductance group (BK_{Ca}) [7]. BK_{Ca} and IK_{Ca} are present in endothelia and vascular SMCs [8], whereas SK_{Ca} is primarily located in the endothelia [9]. Among these channels, BK_{Ca} channels are most prominent in the vasculature [7]. However, there have been no extensive studies on BK_{Ca} channels in the DA.

The BK_{Ca} channel is a tetramer of the pore-forming α subunit encoded by the *KCNMA1* gene with or without four regulatory β subunits [10]. When the intracellular $[Ca^{2+}]$ is lower than 100 nM, BK_{Ca} activity is voltage dependent and independent of intracellular $[Ca^{2+}]$ [11]. Based on their different anatomical distributions, four different β subunit subtypes (β1–4) have been identified, which are encoded by the *KCNMB1–4* genes, respectively [12].

As the BK_{Ca} channel is activated by depolarization and increased intracellular $[Ca^{2+}]$, activation of BK_{Ca} plays an important role in the negative feedback that prevents constant vessel constriction and SMC intracellular calcium overload [13–15]. Recent observations suggest that BK_{Ca} channels play a key role in perinatal pulmonary vasodilation [16, 17]. The purpose of this study is to examine whether the BK_{Ca} α and β subunits and BK_{Ca} currents are present in rat DA, and whether the BK_{Ca} channels are involved in O_2-induced ductal constriction.

Methods

Animal and tissue specimens

Pregnant Wistar rats were purchased from Saitama Experimental Animal Firm. Fetal rats at 19 days of gestation (19D, premature), 21 days of gestation (21D, mature), and full-term newborns (NB) were used. The 19D and 21D fetuses were dissected immediately after cesarean section. The newborns were kept for 1 h at 33°C after delivery by cesarean section, as it is known that neonatal ductal constriction is rapid in the rat, and usually occurs within 1 h after birth [18]. The DA specimens were dissected from the fetuses and newborns after they had been killed with chloroform. Specimens of the DA from fetuses and neonates were rinsed in cold Hank's solution (in mM: NaCl 140, KCl 5.4, NaH_2PO_4 1.2, $MgCl_2$ 0.5, HEPES 10, EGTA 0.1). All experiments were approved by the Ethical Committee of Animal Experiments at Tokyo Women's Medical University.

RNA isolation and quantitative real-time PCR (*qr*-PCR)

Total RNA of the DA was isolated from 150 pooled segments of 19D fetuses, 150 segments of 21D fetuses, and 150 segments of neonates. RNA isolation, cDNA preparation, and *qr*-PCR were carried out according to protocols described previously [19]. Briefly, DNase I digestion of total RNA was carried out on an RNeasy Mini Kit (Qiagen, Germany) extraction column using an RNase-Free DNase Set (Qiagen). The total RNA was reverse-transcribed into cDNA (include 18S rRNA) with random hexamers and MultiScribe Reverse Transcriptase (Applied Biosystems, USA). As a control for genomic DNA contamination, all cDNA synthesis reactions were set up with additional samples lacking reverse transcriptase. BK_{Ca} α and β (β1, 2, 4) primers were designed for *qr*-PCR using Primer Express (Applied Biosystems, USA) (Table 1). The 25 μl *qr*-PCR reaction included 1× Takara SYBR Premix Ex (Takara Bio, Japan), 300 nM of the respective primers, 1× ROX reference dye, and template cDNA corresponding to 1 ng total RNA. 18S ribosomal RNA (Applied Biosystems) was

Table 1 Sequences of primers used in the real-time PCR experiment

Gene	Primer sequences	Amplicon (bp)	Accession no.
Kcnma1 (BK_{Ca} α)			
Forward	CCCAGCCAGTGTACAAAAAGGT	73	NM_031828
Reverse	TCAGGTCTGTCGGTACAAGTTCA		
Kcnmb1 (BK_{Ca} $\beta1$)			
Forward	AAGAGCTGGAGGGCAGGAA	66	NM_019273
Reverse	TGCCCACAGCTGATACATTGA		
Kcnmb2 (BK_{Ca} $\beta2$)			
Forward	GCTCGTACATGCAGAGTGTATGG	79	NM_176861
Reverse	CAGTTAAATGTTTCTGTGATTGACACA		
Kcnmb4 (BK_{Ca} $\beta4$)			
Forward	CGTCCAGGTGTACGTGAACAA	66	NM_023960
Reverse	TGGTGCTGGTCGCTGTGTAG		

used as an internal control. For standard curve production, the plasmids harboring the corresponding BK α and β ($\beta1$, 2, 4) cDNA and ribosomal 18S cDNA fragments were linearized by appropriate restriction enzyme digestion, and then purified, quantified and diluted serially in water containing yeast tRNA (50 ng/μl). Real-time PCR of standards and internal controls was performed each time on the same 96-well plate with the samples to be quantified. To quantify target mRNA expression, cDNA copy numbers were calculated based on the results for the standard curve for the same run. The correlation coefficients were always above 0.99. Each sample was analyzed in triplicate. The cDNA copy numbers were normalized using the calculated 18S cDNA copy number of the same sample.

Immunofluorescence staining and confocal microscope image analysis

The expressions and distributions of the BK_{Ca} α and $\beta1$ subunits were examined in the DA from the 19D, 21D, and NB by following similar protocols to those described previously [20, 21]. Freshly isolated DA specimens were immediately frozen in liquid nitrogen. Frozen sections were prepared with a Leica CM3050 cryostat (Leica Instruments GmbH, Germany). Samples were fixed in 100% methanol, permeabilized in PBS buffer (Sigma, USA) containing 1% Triton X-100, and pre-incubated with 2% donkey serum in PBS at room temperature (RT) for 30 min to reduce non-specific antibody binding. For double immunolabeling, sections were incubated with the primary antibodies of anti-α subunit [anti-K_{Ca} 1.1 (1098–1196) (BK_{Ca}), rabbit, Alomone Labs Ltd., Israel] at 1:300 dilution and anti-alpha smooth muscle actin (α-SMA, mouse, Abcam plc, UK) at 1:400 dilution, a marker of smooth muscle cell, or anti-$\beta1$ subunit (anti-*slo*$\beta1$, rabbit, Alomone Labs Ltd.) at 1:400 dilution and anti-α-SMA at 1:400 dilution and 4°C overnight. Sections were then incubated with 1:500-diluted secondary antibodies for Cy3 (red fluorescence)-conjugated donkey anti-rabbit IgG (Chemicon International, Inc, USA) and for Cy2 (green fluorescence)-conjugated goat anti-mouse IgG (GeneTex, Inc., USA) at RT for 1 h. Negative sections were performed to assure the specificity of the antibodies with the omission of either of the primary antibodies and incubation in buffer only. All staining procedures were performed under the same conditions.

Sections were photographed on an LSM5 PASCAL laser scanning microscope (version 4.0 SP2, Carl Zeiss, Germany). All conditions, including optical sectioning, number of sections and exposures were identical for the same primary antibodies. The intensities of the red fluorescence signals were measured in each image as mean fluorescence intensity values by the LSM5 PASCAL software. The scale of the intensity values ranged from a minimum of 1 (background) to a maximum of 4095 (reddest spot). The relative fluorescence intensity ratio for the α or $\beta1$ subunit in each specimen was computed as the measured value divided by 4095.

Measurement of DA tone

The response of the DA to O_2 is related to fetal gestational age [1, 2]. As the NB DA had already contracted [18], the vascular tensions were measured in 19D and 21D DA rings under the same experimental conditions. The rings (1 ± 0.2 mm) were mounted onto two 40 μm stainless steel wires connected to a force transducer and a micrometer in an organ bath chamber (dual-wire myograph system, model 410A, Danish Myo Technology, Denmark) to measure the isometric tension. Data were recorded with the DMT Normalization Module for Chart™ (ADInstruments, New Zealand). When set up, the chamber was filled with 10 ml Krebs–Henseleit solution (in mM: NaCl 118, KCl 5, $CaCl_2$ 1.5, $MgCl_2$ 1, $NaHCO_3$ 24, NaH_2PO_4 0.436, and glucose 6) at 37°C.

The Krebs–Henseleit solution was equilibrated with either 95% N_2–5% CO_2 (hypoxic) or 95% O_2–5% CO_2 (oxygenated), yielding a final pH of 7.38–7.42, a PCO_2 of 35–42 mmHg, and a PO_2 of 22–25 mmHg (hypoxic solution) or 660–690 mmHg (oxygenated solution), as previously described [20]. Five micrometer indomethacin (Sigma, USA) and 100 μM nitro-L-arginine methyl ester (L-NAME, Sigma) were present in the solution throughout all experiments. These inhibitors of prostaglandin and nitric oxide synthesis were used to study the contractile mechanisms independent of these mediators.

A resting tension was initially applied to each ring in order to obtain the optimal conditions for active tension development [22]. All ductus rings were initially stabilized with hypoxic Krebs–Henseleit solution for 1 h. Paxilline (10–20 μM, Sigma, Germany), a selective inhibitor of the BK_{Ca} α subunit [23], or NS1619 (25–100 μM), a selective activator of the α subunit [23], were added to the hypoxic or oxygenated solution if necessary. In all experiments, we allowed the tension in the rings to reach a new steady-state plateau before the rings were exposed to new experimental conditions.

Electrophysiology

Potassium currents (I_k) were recorded under the whole-cell configuration of the patch clamp technique using an Axopatch 200B amplifier (Axon Instruments, USA) [24]. Freshly isolated DA SMCs from 19D, 21D, and NB were obtained by enzymatic digestion, as previously described [25].

Electrodes were pulled from borosilicate glass (World Precision Instruments, USA) and had a resistance of 3–5 MΩ when filled with the pipette solution (in mM: KCl 140, EGTA 5, $MgCl_2$ 1, Mg-ATP 5, HEPES 5, $CaCl_2$ 1.885, pH 7.2 by KOH, free [Ca^{2+}] 100 nM). The cell suspension was placed into a 1.4 ml chamber on the stage of an inverted microscope (TE200, Nikon, Japan) and perfused (1.8 ml/min) with external solution (in mM: NaCl 140, KCl 4, $MgCl_2$ 1, $CaCl_2$ 2, glucose 10, HEPES 10, pH 7.4 by NaOH) at 37°C in room air. NS1619 (30 μM) or paxilline (1 μM) dissolved in DMSO was added to the external solution if necessary.

The membrane capacitance of single DASMC was determined by applying ramp pulses (first phase: depolarize to −20 mV from a holding potential of 0 mV; second phase: return to the holding potential) at a rate of 1 V/s to avoid interference from any time-dependent ionic currents. I_k were elicited by applying step pulses of voltage. Currents and voltage signals were filtered with a cut-off frequency of 2 kHz, digitized by an A/D converter (DigiData 1200, Axon Instruments), sampled at 1.0 kHz, and recorded and analyzed by pCLAMP 8.2 (Axon Instruments) and Origin 7 (OriginLab Corp, USA) software. The BK_{Ca} currents on DAMSCs from three groups were calculated as the currents measured after the administration of NS1619 minus the currents measured after the administration of paxilline at each voltage step. The current density (pA/pF) of single DASMC was calculated as the current (pA) divided by the capacitance (pF). Current density–voltage curves were obtained by applying voltage steps in 20 mV increments (from −80 to +60 mV) from a holding potential of −70 mV for a duration of 500 ms.

Data analysis

Values are expressed as the mean ± SE in n (number of tests). One-way ANOVA was applied for statistical analysis. Levene's test for equality of variances was performed before the post hoc test. The Bonferroni test was performed in cases with homogeneous variance; otherwise the Dunnett C test was performed. A difference was considered statistically significant when P was less than 0.05.

Results

qr-PCR

The expression of BK_{Ca} α and β1, 2, and 4 transcripts (mRNAs) was detected in the DA from 19D, 21D, and NB (Fig. 1a, b). The amount of α mRNAs present in DA was small (Fig. 1a), while β1 mRNAs were relatively abundant, and β1 was the dominant β subunit in all three groups (Fig. 1b). The α mRNAs in DA decreased by 50% from 19D to 21D and by 70% from 21D to NB (Fig. 1a). The β1 mRNAs in DA increased twofold from 19D to 21D, but decreased by 60% from 21D to NB (Fig. 1b). β2 and β4 mRNAs were also detected in all groups, but only in small amounts (Fig. 1b).

Confocal microscope image analysis

Staining of the rat DA with anti-BK_{Ca} α/β1 and anti-α-SMA antibodies is shown in Fig. 2a and C. BK_{Ca} α (red) and β1 (red) were observed in the tunica intima, media, and adventitia of the DA from 19D, 21D, and NB, while α-SMA (green) was observed in the tunica media. The majority of the α and β1 subunits were colocated with α-SMA in smooth muscle cells (yellow) in all groups (Fig. 2a, c). The staining fluorescence intensity of anti-α antibody was greatest in the 21D and lowest in the NB, and there were significant differences between 21D and 19D and between 21D and NB (Fig. 2b). The fluorescence intensity of anti-β1 antibody was weak in all groups, and there was no significant difference among the three groups

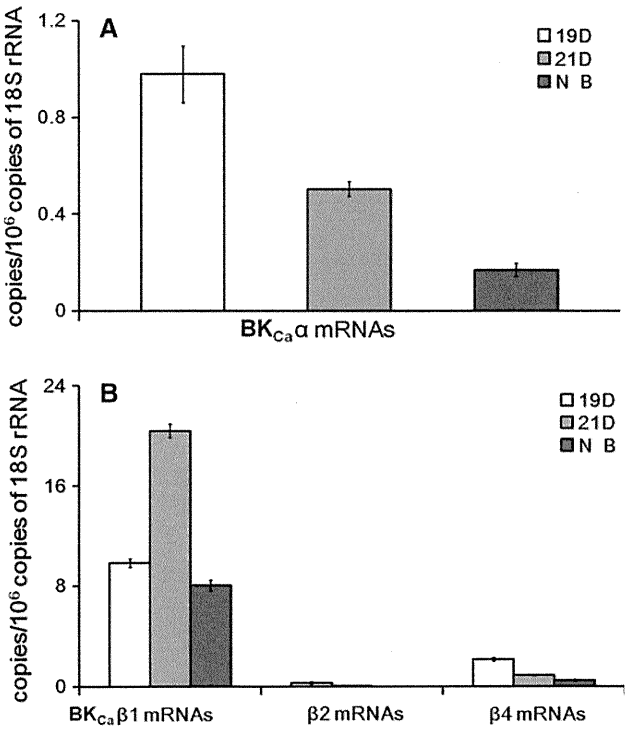

Fig. 1 **a** BK_{Ca} α-subunit transcripts (mRNAs) in the rat DA. The expression of BK_{Ca} α mRNAs was detected in the pooled DA specimens ($n = 150$) from 19D, 21D, and NB. The amount of α mRNAs was small and decreased with advancing development. **b** BK_{Ca} β-subunit transcripts (mRNAs) in the rat DA. The expression of BK_{Ca} β1, 2, and 4 mRNAs was detected in the pooled DA specimens ($n = 150$) from 19D, 21D, and NB. The β1 subunit was the dominant β subunit in the DA from all age groups, and it was relatively abundant in the 21D DA. A small amount of β2 mRNAs and a few β4 mRNAs were also detected

(Fig. 2d). Negative control sections treated only with secondary antibodies or buffer did not show any staining (data not shown).

Measurement of term DA tone

Representative recordings of the DA tone are shown in Fig. 3. The oxygenated solution induced obvious constriction in the 21D DA but only slight constriction in the 19D DA (Fig. 3a, b).

Neither immature nor mature DA rings were sensitive to paxilline. Paxilline (10–20 μM) did not increase the 19D and 21D ductus tone under hypoxic conditions (Fig. 3a). 21D ductus tension increased in the oxygenated solution in the presence of paxilline (20 μM) to a similar degree as in the absence of paxilline (Fig. 3a). When the 19D and 21D ductus rings had already been constricted under oxygenated conditions, paxilline (10–20 μM) failed to increase their tensions further (Fig. 3a).

NS1619 (25–100 μM) did not alter the resting tensions of either 19D or 21D DA in hypoxic solution (Fig. 3b). O_2 failed to increase 21D DA tension notably when the ring was preincubated with NS1619 (100 μM), but the response of 19D DA to O_2 was unaffected after preincubation (Fig. 3b). The O_2 sensitivity of the 21D DA was restored after NS1619 had been washed out (Fig. 3b). NS1619 (25–100 μM) attenuated 21D DA tension in a dose-dependent manner under oxygenated conditions. NS1619 did not cause vasodilation in the 19D DA under the same conditions (Fig. 3b). Higher concentrations of paxilline or NS1619 did not alter the DA tensions any further in any experiment.

Electrophysiology

The effects of NS1619 and paxilline on I_K were tested in DASMCs isolated from 19D, 21D, and NB, respectively. The I_K was obtained in the DASMCs when the voltage was clamped above +20 mV. I_K was enhanced by NS1619 (30 μM) and suppressed by paxilline (1 μM). The maximal I_K was obtained at a voltage of +60 mV in all groups. Representative I_K traces recorded at +60 mV in a single DASMC from each group as well as the current density (pA/pF) versus voltage (mV) curves are shown in Fig. 4a, b, respectively. No BK_{Ca} currents were detected in the DASMCs at negative potential in any group (Fig. 4b). The NS1619/paxilline-sensitive potassium (BK_{Ca}) current density invoked at +60 mV in the DASMC was greatest in the 21D and smallest in the NB, and there were significant differences between 21D and 19D and between 21D and NB (Fig. 4b).

Discussion

A better understanding of the mechanisms of ductal contraction and relaxation has major clinical implications. Michelakis et al. [26] have studied the K_V and BK_{Ca} channels in DA isolated from human neonates. Their results showed that the inhibition of K_V channels, but not BK_{Ca} channels, resulted in ductal constriction under hypoxic conditions. However, as BK_{Ca} channels are sensitive to membrane depolarization and an increase in intracellular $[Ca^{2+}]$, which occur in DASMCs upon the elevation of PO_2, it is possible that BK_{Ca} channels may be activated in the DA under oxygenated conditions. In the present study, developmental changes in the BK_{Ca} (both α and β1) channels in rat DA from 19D (immature) to 21D (mature) and NB (after birth) were studied in order to better understand their roles in the regulation of DA tone.

BK_{Ca} α mRNAs and protein were detected in the DA in all age groups (Figs. 1a, 2a, b), suggesting the presence of BK_{Ca} channels in the rat DA. The four family members of β subunits are differentially expressed in various tissues,

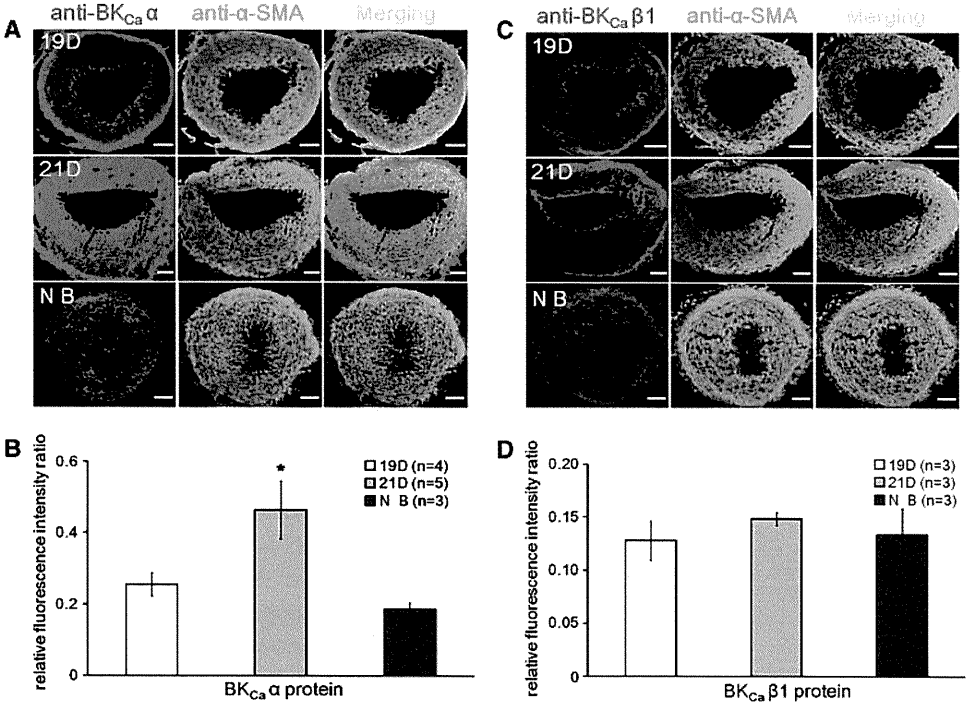

Fig. 2 **a** The staining of the rat DA with anti-BK_{Ca} α and anti-α-SMA antibodies. BK_{Ca} α subunits (*red*) were observed in the tunica intima (endothelia), media (SMCs), and adventitia of the DA from 19D, 21D, and NB, while α-SMA (*green*) was located in the tunica media in all specimens. The majority of the α subunits were colocated with the α-SMA in SMCs (*yellow*) in all three groups. The fluorescence intensity of the α subunits was strong in all age groups, especially in the 21D DA. *Bar length* 50 μm. **b** The relative fluorescence intensity ratio of the BK_{Ca} α subunits in the rat DA. The relative fluorescence intensity ratio of the α subunits was greatest in 21D, and lowest in NB. $^*P < 0.05$ compared with 19D or NB. **c** The staining of the rat DA with anti-BK_{Ca} β1 and anti-α-SMA antibodies. BK_{Ca} β1 subunits (*red*) were observed in all layers of the DA from 19D, 21D, and NB. The majority of the β1 subunits were colocated with α-SMA (*green*) in SMCs (*yellow*) in all three groups. The fluorescence intensity of the β1 subunit was similarly weak in all three groups. *Bar length* 50 μm. **d** The relative fluorescence intensity ratio of the BK_{Ca} β1 subunits in the rat DA. There was no significant difference in the relative fluorescence intensity ratios of the β1 subunits among the three groups

including β1 in SMCs, β2 in kidneys, β3 in the placenta, and β4 in the brain [12]. The β1 subunit is expressed predominantly in vascular SMCs [12]. Our *qr*-PCR results confirm that β1 is the dominant β subunit in the rat DA (Fig. 1b).

Although BK_{Ca} channels were detected in the endothelium and adventitia, the majority of the BK_{Ca} channels were located in the DASMCs, as demonstrated by their colocalization with α-SMA in all groups (Fig. 2a, c). The BK_{Ca} current was greatest in the mature DASMC (Fig. 4a, b), as the protein expression of the α subunit was greatest in the mature DA (Fig. 2a, b). However, there was a discrepancy between mRNA levels and protein levels in the rat DA in the three groups (Figs. 1, 2). The mode of mRNA and protein or functional changes may not always be the same [27]. This discordance could be due to variance in post-transcriptional modulations of mRNAs, splice variants, ribosome and aminoacyl tRNA amounts, translation kinetics, or protein stability at different developmental stages [28, 29].

In order to examine whether BK_{Ca} channels are involved in O_2-induced ductal constriction, we measured rat DA tensions under various conditions. Mature DA rings exhibited a high sensitivity to O_2, while immature DA showed little response to O_2 (Fig. 3a, b). This indicates that the contractile components that prepare the DA for the increase in PO_2 are well developed in the mature DA, but are underdeveloped in the immature DA.

Paxilline had no effect on the 19D DA or the 21D DA under either hypoxic or oxygenated conditions (Fig. 3a). If BK_{Ca} channels are active in the DA under hypoxic conditions and O_2 inhibits BK_{Ca} channels, contributing to O_2-induced ductal constriction, paxilline would be expected to augment the ductus tone under hypoxic conditions. In the present study, paxilline failed to increase 19D and 21D DA tension under hypoxic conditions (Fig. 3a), suggesting that the BK_{Ca} channels in both immature and mature DA were inactive under hypoxic conditions. Furthermore, the 21D ductus tone increased in the oxygenated solution in the presence of paxilline to the same extent as in the absence of paxilline (Fig. 3a). These data suggest that O_2-induced DA constriction is not due to the inhibition of BK_{Ca} channels.

On the other hand, it is possible that BK_{Ca} channels in the mature DA are activated under oxygenated conditions,

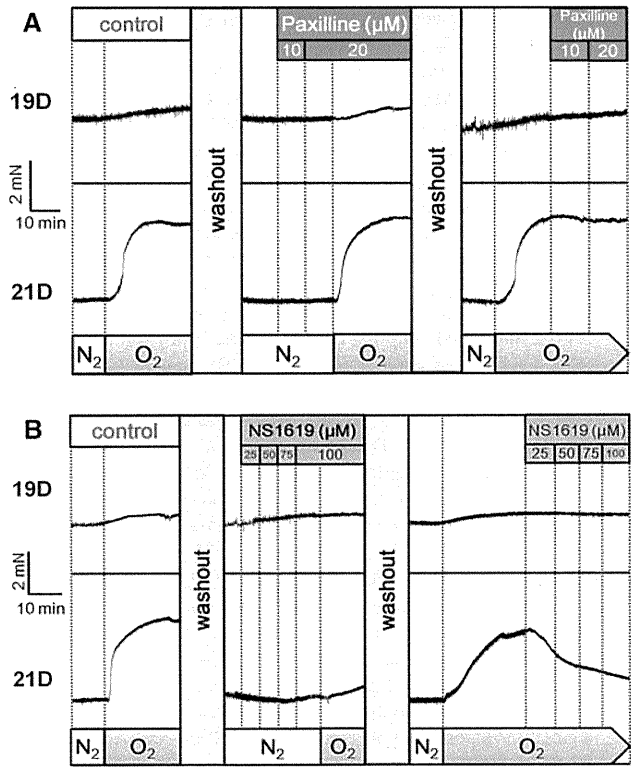

Fig. 3 **a** The effects of paxilline on the rat DA under hypoxic and oxygenated conditions. O_2 induced remarkable constriction (≈3 mN) in the 21D DA but only slight constriction (≈0.5 mN) in the 19D DA. Paxilline (10–20 μM) did not increase either 19D or 21D ductus tone under hypoxic or oxygenated conditions. 19D and 21D ductus tensions increased in oxygenated solution in the presence of paxilline (20 μM) to the same extent as in the absence of paxilline. *mN* millinewtons. **b** The effects of NS1619 on the rat DA under hypoxic and oxygenated conditions. NS1619 (25–100 μM) did not alter the resting tension of the 19D and 21D DA under hypoxic conditions. O_2 failed to increase the 21D DA tension notably when the ring was preincubated with NS1619 (100 μM), but the response of the 19D DA to O_2 was unaffected under the same conditions. The O_2 sensitivity of the 21D DA was restored after the NS1619 had been washed out. NS1619 (25–100 μM) attenuated the 21D ductus tension in a dose-dependent manner under oxygenated conditions. NS1619 did not dilate the 19D DA under the same conditions. *mN* millinewtons

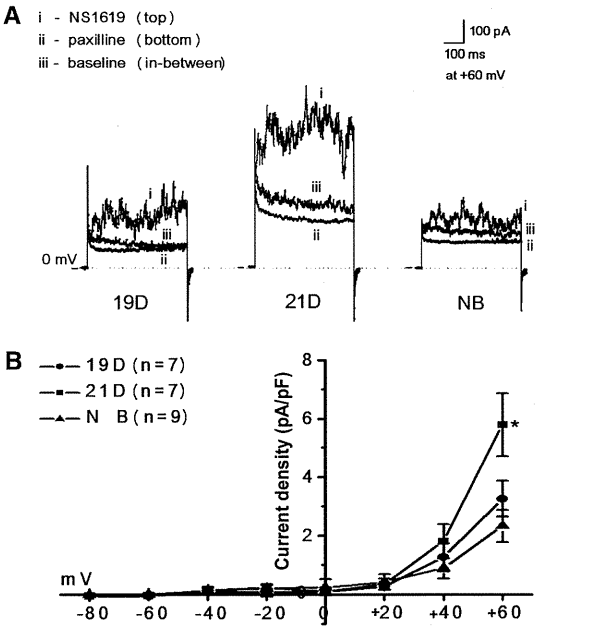

Fig. 4 **a** Representative I_K traces recorded in single DASMCs from 19D, 21D, and NB at a voltage of +60 mV. For each DASMC, the middle trace (*iii*) represents the I_K recorded in the external solution as a baseline; the top trace (*i*) was recorded after NS1619 (30 μM) had been applied in the external solution; and the bottom trace (*ii*) was recorded after paxilline (1 μM) had been applied in the external solution. The I_K values recorded in the 21D were much greater than those seen in the 19D and NB. **b** Current density (pA/pF) versus voltage (mV) curves for the rat DASMCs. The BK_{Ca} currents in the DASMCs from all age groups were obtained when the voltage was above +20 mV. No BK_{Ca} currents were detected at negative potential in the DASMC for any group. The maximal BK_{Ca} currents in all groups were obtained at a voltage of +60 mV, and were greatest in 21D and smallest in NB. $^*P < 0.05$ compared with 19D or NB

as the BK_{Ca} channels may be activated by depolarization and increased intracellular $[Ca^{2+}]$ in DASMCs. However, paxilline failed to further increase the 21D ductus tone under oxygenated conditions (Fig. 3a). This suggests that that BK_{Ca} channels are not activated in DA preconstricted by O_2. Even though membrane depolarization (up to −20 mV) occurs in the DASMCs under oxygenated conditions [6], such depolarization is not adequate to activate BK_{Ca} channels, because no BK_{Ca} currents were detected from the rat DASMCs at negative potential (Fig. 4b). Although the intracellular $[Ca^{2+}]$ was not measured in DASMCs in this study, it has been reported that the $[Ca^{2+}]$ increased (nM range) in the depolarized DASMC [4]. This level was much lower than the concentration (μM range) required to effectively activate BK_{Ca} channels [30]. All of the data indicate that BK_{Ca} channels in the mature as well as immature DA stay inactive even when the DA is constricted under oxygenated conditions. In other words, BK_{Ca} channels are not involved in O_2-induced ductal constriction.

NS1619 induced vasodilatation in the 21D DA preconstricted by O_2, but it did not dilate the 19D DA under oxygenated conditions (Fig. 3b). This indicates that there were more BK_{Ca} (α) channels in the mature DA than in the immature DA. This finding is consistent with the protein (Fig. 2b) and current (Fig. 4) results. Although NS1619 did not change the resting tension of the 21D DA in hypoxic solution (Fig. 3b), preincubation with NS1619 weakened the O_2 sensitivity of the mature DA (Fig. 3b). In addition, NS1619 dilated the preconstricted 21D DA dose dependently under oxygenated conditions (Fig. 3b). This indicates that BK_{Ca} channels can be activated in the mature DA under hypoxic as well as oxygenated conditions.

The physiological significance of developmental changes in the BK_{Ca} channel is not clear. Although the present